Structural and Multidisciplinary Optimization (2024) 67:22
https://doi.org/10.1007/s00158-023-03732-4

RESEARCH PAPER

Manufacturability-aware deep generative design of 3D metamaterial units for additive manufacturing

Zihan Wang[1] · **Hongyi Xu**[1]

Received: 24 July 2023 / Revised: 14 December 2023 / Accepted: 22 December 2023 / Published online: 14 February 2024

Abstract

Mechanical metamaterials are artificial structures that possess exceptional mechanical properties that are not naturally occurring. The complex geometrical and topological features of these metamaterials pose significant challenges to both structure design and manufacturing, despite the recent rapid development of additive manufacturing (AM) techniques. Thus, an effective framework for designing 3D metamaterials with desired mechanical properties, while also ensuring AM manufacturability, is urgently needed. In this paper, an AM manufacturability-aware deep generative model-based design framework is proposed for designing 3D metamaterial units for target properties. To accomplish this, we propose using Variational Autoencoder (VAE) as the feature extractor, which maps the 3D metamaterial geometries to a low-dimensional latent feature space. The latent feature space is concurrently linked to discriminators/regressors to predict manufacturability metrics and mechanical properties. We demonstrate that the proposed design framework is capable of designing high-performance metamaterial units with various user-defined manufacturability metrics. To showcase the effectiveness of the proposed design framework, three design cases with different objective functions are presented, and the final optimal designs are validated by comparing them to state-of-the-art designs or the optimal designs obtained by topology optimization methods.

Keywords Metamaterial · Deep generative design · Manufacturability · Image analysis · VAE · Property-driven design

1 Introduction

Mechanical metamaterials are artificial structures that possess exceptional mechanical properties, such as having unique stiffness-to-weight ratio (Zheng et al. 2014), acoustic damping (Chen and Chan 2007), wave trapping (Wang et al. 2021, 2022a, 2022b; Gurbuz et al. 2021), vibration damping (Claeys et al. 2017; Garland et al. 2020; Qian et al. 2021), and energy absorption properties (Alberdi et al. 2020; Liu et al. 2020; Xu and Liu 2019). The superior mechanical properties originate from the architectural features of the metamaterial units. Owing to their superior mechanical properties, mechanical metamaterials have great potential for application in aerospace, seismic engineering, biomechanics and medical devices, sports equipment, and various other fields. However, the complexities inherent in controlling the geometry and topology of metamaterial units, intricate nonlinear properties that necessitate advanced computational methods, and the challenges related to manufacturing all present obstacles in their design and production. The advancements in manufacturing techniques have facilitated the development of metamaterials with complex geometric features. In particular, additive manufacturing (AM) (Bodaghi et al. 2017; Lei et al. 2019) has great potential in fabricating metamaterials with complex shapes that were previously impossible to produce using traditional manufacturing techniques (Li et al. 2016; Pham et al. 2019; Thompson et al. 2016). Despite the greater design flexibility that AM provides, it is still crucial to incorporate AM-related manufacturability constraints, such as support structure (Jiang et al. 2018; Strano et al. 2013), powder removal (Hunter et al. 2020), and process-specific metrics (Oliveira et al. 2020), into the structure design process. The current structure design for AM processes inadequately accounts for the interdependence between metamaterial design and AM manufacturing.

Responsible Editor: Palaniappan Ramu

✉ Hongyi Xu
hongyi.3.xu@uconn.edu

[1] School of Mechanical, Aerospace, and Manufacturing Engineering, University of Connecticut, Storrs, CT 06269, USA

To address this issue, several approaches that consider part manufacturability have been proposed in the literature. A widely used approach is the real-time process monitoring (Grasso and Colosimo 2017; Qi et al. 2019), which utilizes image-based monitoring techniques to detect potential failures during the printing process and alert the user before the process completes. However, this approach still falls short of improving the manufacturability of the part during the design stage. Regarding the design for manufacturability approaches, one straightforward approach is to provide a design worksheet as a reference for the engineers to evaluate their designs (Booth et al. 2017). However, this manual approach is time-consuming and limited to the predefined criteria listed in the worksheet. Tedia and Williams (2016) proposed a voxel-based manufacturability analysis approach that checks the manufacturability based on the minimal feature size, support material, orientation, and manufacturing time for different build orientations. Shi et al. (2018) introduced a feature-based method using heat kernel signature for manufacturability analysis in AM, including unsupported feature, minimum feature size, minimum self-supporting angle, and minimum vertical aspect ratio. Telea and Jalba (2011) proposed a voxel-based, distance fields metrics manufacturability analysis technique for thin-region detection. Kerbrat et al. (2011) proposed a method that decomposes the geometrical model into octrees and evaluates the manufacturability index of each octant. Despite these efforts, these methods still lack the capability of enhancing the manufacturability of the part during the design stage based on the user-defined metrics. Therefore, a metamaterial design methodology that incorporates AM manufacturability is highly desired. Manufacturability checking is also implemented in commercial software, including Magics, Nettfab, and online 3D printing service, such as 3DXpert, Sculpteo, and Shapeways. They provide functions such as identifying and evaluating the minimum feature size based on the printer's resolution, optimizing the build orientation, and generating and measuring support structures. However, these functions are often specific to a particular type of printer and have limited capability to handle various types of features. For instance, some software may not be able to detect enclosed voids.

Topology optimization (TO) has emerged as a powerful computational tool that optimizes an objective function subject to different constraints, by recasting the design problem as an optimal material distribution problem in a specific design domain. Topology optimization has been recently applied to design structures with complex geometrical features that are suitable for AM. Manufacturability metrics, such as overhang angle (Qian 2017; Zhang et al. 2022b), overhang length (Zhang et al. 2022a), enclosed void (Xiong et al. 2020; Zhou and Zhang 2019), and feature size (Bostanabad et al. 2019), are considered in topology optimization formulations for designing additively manufactured structures. However, previous works only considered one or two of those manufacturability metrics and a comprehensive topology optimization methodology that addresses all the mentioned manufacturability criteria is currently lacking. There are also a few works on topology optimization for designing AM metamaterials (Gao et al. 2018; Li et al. 2018; Takezawa et al. 2017; Wang et al. 2014; Zhang and Khandelwal 2020). Vogiatzis et al. (2017, 2018) proposed a level-set method-based TO for designing negative metamaterials with Poisson's ratios. However, the obtained optimal 3D designs were extruded from the 2D units to ensure AM manufacturability, which greatly limits the design scope to a 2D design space. Watts et al. (2019) proposed a surrogate modeling-based method for designing macroscale structures infilled with metamaterials. However, in this work, only the connectivity between two different unit cells was considered in terms of the manufacturability. Takezawa et al. (2017) proposed a topology optimization framework to obtain the optimal metamaterial unit design with high stiffness and verified it experimentally. This research considered two AM manufacturability metrics: the absence of enclosed voids and the minimization of inclined shapes within the metamaterial structures. However, these metrics were not directly included in the design formulation. Instead, holes with fixed diameters and locations were pre-defined in the design space to ensure the absence of enclosed voids. The works mentioned above only incorporated a limited set of manufacturability metrics, limiting the generalizability of the proposed design approaches. Moreover, incorporating AM manufacturability into TO is challenging because the metrics need to be differentiable for gradient-based optimization. Thus, it is difficult to perform manufacturability analysis on voxel-based or slice-based 3D metamaterial structures. Consequently, integrating AM manufacturability analysis with TO for metamaterial unit design is still a significant challenge.

Deep learning (DL) has shown significant promise in the field of computational metamaterial design (Yang et al. 2018; Liu, et al. 2016; Jha et al. 2018; Cang et al. 2017; Wang et al. 2020b, 2022a; Meyer et al. 2022; Bastek et al. 2022; Kumar et al. 2020) and there have been a few attempts to leverage the synergy of DL and AM techniques in this area. For instance, Wilt et al. (2020) proposed a DL-based surrogate modeling method for the prediction of errors in compliant auxetic metamaterials produced by additive manufacturing. Zeng et al. (2022) developed a DL-based design method for the inverse design of multiscale, multifunctional, and gradient mechanical metamaterial while considering the compatibility between adjacent units as an AM manufacturability metric. Gu et al. (2018) proposed a convolutional neural network-based design approach for designing hierarchical materials. The designed structures were fabricated and validated by multi-material jetting AM process.

Zeng et al. (2023) proposed a deep learning approach for the inverse design and 3D printing of gradient mechanical metamaterials. However, their method was limited by the creation of 3D metamaterial units through the extrusion of 2D metamaterials, restricting the design scope to the 2D space. Although DL-based design methods have been successful in generating novel designs that can be fabricated using AM, they have not explicitly considered or only considered a limited number of AM manufacturability metrics during the design process. As a result, there is no guarantee that these optimized designs can be manufactured efficiently.

Previous methods of designing metamaterial units either included only a restricted range of manufacturability metrics or did not explicitly integrate manufacturability metrics, thereby constraining the flexibility and generalizability of these approaches. The motivation of this research is to address limitations in previous research works of designing 3D metamaterial units. The goal of this research is to design high-performance 3D metamaterial units that meet various manufacturability constraints. To accomplish this, we propose an integrated manufacturability-aware deep generative design framework comprising two major components: (1) a unified manufacturability-aware deep generative model for feature learning and (2) a design optimization approach for generating 3D metamaterial units for optimal properties while considering manufacturability constraints. The framework considers three design objectives, which are elastic modulus, Poisson's ratio, and heat conductivity, and six manufacturability metrics, including surface area, maximum feature size, minimum feature size, minimum overhang angle, maximum overhang length, and enclosed voids. Users can selectively enable or disable these design objectives and manufacturability metrics to obtain 3D metamaterial units with varying performances and manufacturability-related geometric characteristics.

The major contributions of this work are summarized as follows:

(1) An image analysis-based approach is proposed for evaluating AM manufacturability metrics based on voxelated 3D metamaterial units. This approach can be easily extended for applications on any other voxel-based 3D structures.
(2) A manufacturability-aware deep generative model is established to learn a unified feature space that incorporates geometrical, manufacturability, and mechanical properties information.
(3) The proposed design framework exhibits both flexibility and generalizability in multi-objective design of 3D metamaterial units for multiple properties, as well as accommodating multiple manufacturability metrics. The resulting 3D metamaterial unit successfully complies with various manufacturability constraints.

The structure of this paper is as follows. In Sect. 2, we describe the process of creating a highly diverse 3D metamaterial database, which includes geometry information as well as associated mechanical properties, such as elastic modulus, Poisson's ratio, and heat conductivity. We also define and evaluate the manufacturability metrics by conducting image analysis on the metamaterial unit samples. Section 3 proposes an integrated manufacturability-aware deep generative model-based design framework. In Sect. 4, we demonstrate the effectiveness of the proposed design approach through one unsupervised and three supervised design cases. Finally, in Sect. 5, we summarize the contributions of this work and discuss potential future research directions.

2 Establishment of the metamaterial database: metamaterial unit geometry, mechanical properties, and manufacturability metrics

2.1 Generation and collection of 3D metamaterial units

In total, we created a highly diverse database that consists of 46,840 metamaterial unit samples. The 3D metamaterial units are generated or collected from three different methods/resources. All the metamaterial unit samples have a resolution of $48 \times 48 \times 48$ voxels.

The first group of 3D metamaterial units are generated using the microstructure family template-based method that is modified from the one proposed in literature (Chen et al. 2018). The structures are defined in a cubic space, and the structure geometries are enforced to be cubic symmetric by constraining structures inside a single control tetrahedron (red-dotted area) and mirroring it to 48 copies. The detailed generation process can be found in Appendix A1. Any structures generated by this method that consist of disconnected components rather than a single contiguous part, not connected to the neighbor units under the periodic boundary condition (PBC) or having a volume fraction outside the range of $[0.05, 0.4]$ are removed from the generated dataset. Some examples of 3D metamaterial units generated are shown in Fig. 1a.

The second group of 3D metamaterial units are generated by defining the skeletons of the cubic symmetric metamaterial unit in a continuous design domain and then creating the geometries by assigning radius (r) along the skeleton. This group contains octet structures, octahedral structures, and body-centered cubic structures. Some examples in this group are shown in Fig. 1b.

The last group of 3D metamaterial units are collected from the open source dataset (Chan et al. 2021). This metamaterial group is generated using level-set functions, which

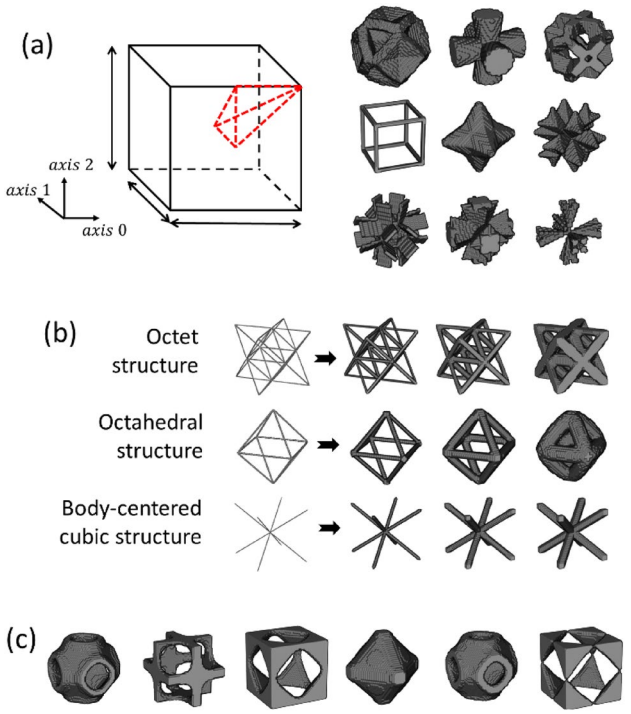

Fig. 1 **a** The cubic region defining cubic symmetric metamaterial units and a few examples of 3D metamaterial units generated using the first method. **b** A few examples from the second group: octet structures, octahedral structures, and body-centered cubic structures. **c** A few examples of the 3D metamaterial units collected from Chan et al. (2021)

create isosurface families based on crystallographic structure factors. We only select the cubic symmetric metamaterial units with volume fraction in the range of $[0.05, 0.4]$. It is to be noted that the metamaterial unit samples from open source dataset only provide the shape information, while a parametric description of each sample is not available. Examples from the third group are shown in Fig. 1c.

Because of the substantial diversity in structural characteristics and the distinct nature of the generation algorithms, representing all metamaterial unit samples with a limited set of geometric parameters is unfeasible.

2.2 Mechanical properties simulation

In this research, we will showcase the design approach by exploring two different properties of metamaterial units: elasticity and heat conductivity. To illustrate the methodology, we have selected aluminum as the base material, which has elastic properties of $E_{\text{Al}} = 68300\text{MPa}$ and $\nu_{\text{Al}} = 0.31$ and heat conductivity of $k_{\text{Al}} = 0.237\,\text{W/mmK}$. This framework has the potential to be extended to other base materials, such as steel, titanium, copper, and Inconel. However, simulations of the metamaterial unit properties will need to be reconducted using the new material properties.

The elastic properties are obtained by finite element simulation in ABAQUS with unified PBC (Xia et al. 2003). The cubic symmetric of 3D metamaterials ensures that all structures have elastic tensors with only three parameters: elastic modulus E, Poisson's ratio ν, and shear modulus G. As a result, the effective stress–strain tensor $\boldsymbol{C}^{eff}$ is expressed as follows:

$$\boldsymbol{C}^{eff} = \begin{bmatrix} \frac{E(1-\nu)}{(1+\nu)(1-2\nu)} & \frac{E\nu}{(1+\nu)(1-2\nu)} & \frac{E\nu}{(1+\nu)(1-2\nu)} & 0\ 0\ 0 \\ \frac{E\nu}{(1+\nu)(1-2\nu)} & \frac{E(1-\nu)}{(1+\nu)(1-2\nu)} & \frac{E\nu}{(1+\nu)(1-2\nu)} & 0\ 0\ 0 \\ \frac{E\nu}{(1+\nu)(1-2\nu)} & \frac{E\nu}{(1+\nu)(1-2\nu)} & \frac{E(1-\nu)}{(1+\nu)(1-2\nu)} & 0\ 0\ 0 \\ 0\ 0\ 0 & & & G\ 0\ 0 \\ 0\ 0\ 0 & & & 0\ G\ 0 \\ 0\ 0\ 0 & & & 0\ 0\ G \end{bmatrix} \tag{1}$$

The stress–strain tensor $\boldsymbol{C}^{eff}$ can be extracted by solving the stress–strain relationship using the output of the ABAQUS simulation.

Thermal conductivity is a property that characterizes the ability of the material to conduct heat when a temperature load or temperature gradient field is applied to the design domain. The thermal conductivities of 3D metamaterial units are simulated in ABAQUS under PBC (Mirabolghasemi et al. 2019). For 3D cubic symmetric metamaterials, effective thermal conductivity tensor $\boldsymbol{K}^{eff}$ can be written as a 3×3 matrix based on isotropic thermal conductivity k (Eq. 2). The $\boldsymbol{K}^{eff}$ is extracted from the output of the ABAQUS simulation. Therefore, the thermal conductivity k can be obtained.

$$\boldsymbol{K}^{eff} = k \begin{bmatrix} 1\ 0\ 0 \\ 0\ 1\ 0 \\ 0\ 0\ 1 \end{bmatrix} \tag{2}$$

For each metamaterial unit, its elastic modulus E, Poisson's ratio ν, and thermal conductivity k are obtained by simulation. The histograms in Fig. 2a show the statistics of the three mechanical properties of all samples in the metamaterial database.

2.3 Manufacturability evaluation by image analysis

There is no universal set of manufacturability metrics that applies to all AM techniques, as the requirements of the printing process and part geometries vary depending on the specific technique used. Therefore, the proposed framework incorporates a set of widely applicable geometry-based manufacturability metrics and can be extended to include additional metrics that are specific to particular AM techniques and part geometries. Image analysis algorithms/tools are developed in MATLAB to evaluate AM manufacturability metrics based on the voxel images of metamaterial samples (Ashburner and Friston 2000).

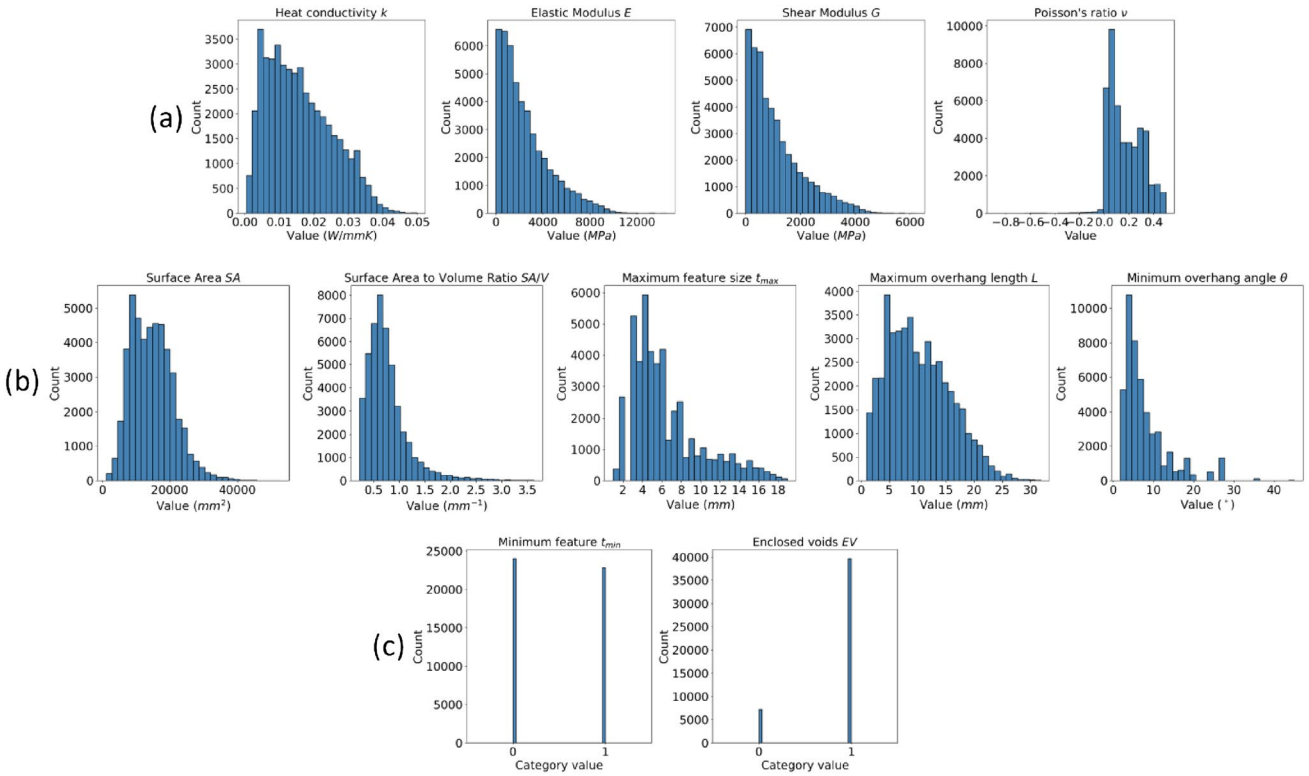

Fig. 2 **a** Statistics of the heat conductivity, elastic modulus, and Poisson's ratio of all 3D metamaterial unit samples in the database. **b** Statistics of the continuous manufacturability metric values of all samples. **c** Statistics of the binary manufacturability metric values of all samples

2.3.1 Surface area (SA) and surface area-to-volume ratio (SA/V)

In AM, both surface area and surface area-to-volume ratio of a 3D-printed part are critical factors affecting the quality and properties of the final product. When the surface area is large, the part tends to cool more rapidly, resulting in increased residual stresses and distortions (Tao and Leu 2016). Furthermore, a larger surface area can lead to increased exposure to oxygen, which can alter the microstructure and mechanical properties of the material (Yadollahi and Shamsaei 2017). Additionally, in certain printing techniques, such as selective laser sintering (SLS) or binder jetting (BJ), a high surface area can cause the part to adhere more strongly to the build plate, making it difficult to detach and increasing the risk of damage to the part or build plate. Surface area-to-volume ratio is often used to assess the compactness and efficiency of a design. A lower SA/V indicates less material usage, which is suitable for lightweight design. In opposite, a higher SA/V often associated with complex geometries, which may require support structures during printing to maintain their stability. Additionally, in metal additive manufacturing processes like powder bed fusion (PBF) and selective laser sintering (SLS), a high SA/V can lead to uneven powder distribution within the build chamber, potentially affecting the density and properties of the printed part.

2.3.2 Maximum overhang length (L) and minimum overhang angle (θ)

Due to the layer-by-layer building characteristic of AM processes, the overhang features are a major limitation, particularly in material extrusion techniques (Zhang et al. 2020). Previous research has shown that unsupported overhang features can lead to a deterioration in shape accuracy, mechanical properties, and surface quality (Atzeni and Salmi 2015; Feng et al. 2021; Thore et al. 2019). Support structures are typically used to successfully print overhang structures, but they increase printing time and post-processing complexity (Järvinen et al. 2014; Wei et al. 2019) and can lead to rough surfaces and decreased structural integrity (Lam et al. 2020). Therefore, reducing the maximum overhang length can help to minimize the need for total support structures and improve printing efficiency.

Overhang analysis is based on a voxelated model shown in Fig. 3a, where i denotes the i^{th} layer of an overhang, counting from the bottom to the top. L_i represents the width of an overhang part without support beneath it in the i^{th} layer. Among all the L_i values, we define the maximum L_i as the

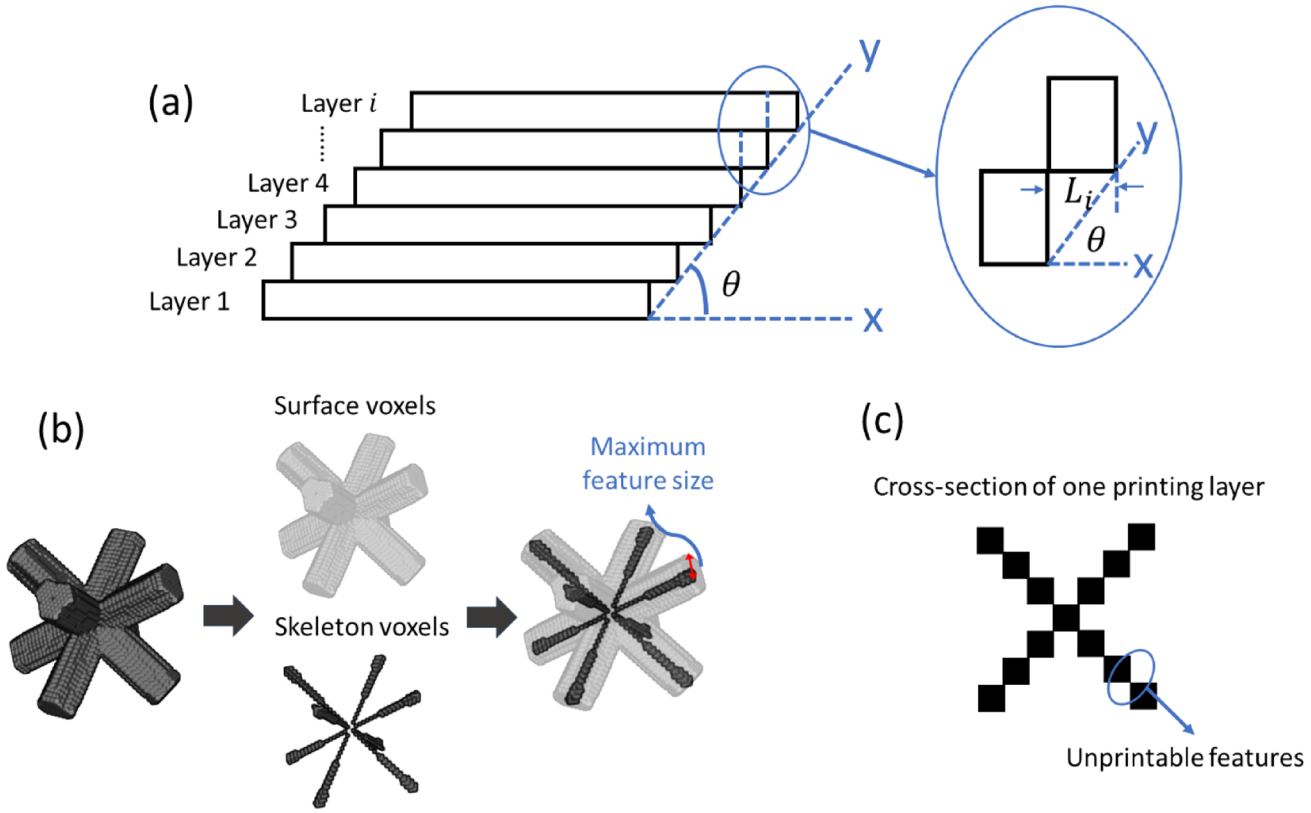

Fig. 3 **a** Definition of the overhang angle and the maximum overhang length. **b** Definition of the maximum feature size. **c** Definition of unprintable minimum features

maximum overhang length L. In addition to minimizing the overhang length, another strategy to reduce the need for support structures is to minimize the overhang angle. The minimum overhang angle θ is defined as the angle between the x–y plane, as illustrated in Fig. 3a, that can be fabricated without adding support during the deposition process. The overhang angle is an important factor to consider in additive manufacturing techniques, particularly those that use support structures, such as fused deposition modeling (FDM) (Bintara et al. 2019), stereolithography (SLA) (He and Song 2018), and selective laser sintering (SLS) (Kruth et al. 2005). Typically, θ is set at 45° (Jin et al. 2017; Wei et al. 2016). However, the optimal angle may vary for different printers and materials, and some researchers may perform tests to determine the suitable angle size before printing the part (Lee and Lee 2017).

2.3.3 Maximum feature size (t_{max})

The size of features in a 3D-printed part is an important consideration for AM, as overly thick features can be susceptible to distortion for certain techniques. For example, in metal binder jetting (BJ) techniques, thicker parts can be more difficult to bind uniformly, resulting in areas with higher binder content that may not be burned off completely during sintering (Lores et al. 2019). This can lead to residual stresses in the part, which can cause warping or distortion. In laser-based AM techniques, such as selective laser melting (SLM) and powder bed fusion (PBF), a thicker part may receive a higher laser power to ensure complete melting of the material. However, increasing the laser power can also result in greater heat accumulation and potential distortion or cracking (Li et al. 2017). While there is no widely accepted maximum feature size (Reddy et al. 2016), we include it as one of the manufacturability metrics for the prospective users. In this work, the maximum feature size is obtained by the following procedure. One illustrative example of the maximum feature size is shown in Fig. 3b.

(a) Find the skeleton of the structure, which is in the format of voxel image. Record the skeleton as solid voxels.
(b) For each solid voxel in the skeleton, calculate its shortest distance to the surface of the structure. Record all the distances as a list.
(c) Find the maximum value in the list. The maximum value corresponds to the maximum feature size t_{max}.

2.4 Minimum feature size (t_{min})

Minimum feature size is one of the most important manufacturability metrics, which, in practice, is limited not only by the laser spot size and powder size, but also by the 3D model slicing and resolution of the machine (Moylan et al. 2012; Tedia and Williams 2016). The minimum feature size is considered for various AM techniques, such as stereolithography, inkjet printing, selective laser sintering, and binder printing (Bertrand et al. 2007; Boschetto and Bottini 2014; Cao et al. 2015). In this work, we consider the edge/corner-connected voxels (Fig. 3c) as the unprintable features due to the bottleneck shape between the two voxels. The minimum feature size is obtained by the following procedures:

(a) Slice the 3D metamaterial unit layer by layer, in this work, each layer has a thickness of one voxel. Therefore, we slice the 3D metamaterial unit into 48 pieces in total.
(b) For each piece, identify and record the number of connected voxels at edges and corners. This process is iterated over all 48 pieces.
(c) Sum up the number of edge/corner-connected voxels for all the layers. If the number is greater than 0, the structure is considered to have unprintable minimum features and is categorized as 1. Otherwise, the structure is categorized as 0, indicating that it does not have unprintable minimum features.

2.4.1 Enclosed voids (EV)

Enclosed voids have negative impacts on both the powder-based and material extrusion-based AM techniques, such as selective laser sintering (SLS) (Tuncer and Bose 2020; Wang et al. 2020a), fused deposition modeling (FDM) (Hutmacher et al. 2001; Zein et al. 2002), and electron beam melting (EBM) (Walton and Moztarzadeh 2017). In powder-based techniques, unsintered powder acts as a support material that must be removed after fabrication. In material extrusion-based techniques, support structures may also be necessary and need to be removed after fabrication. Therefore, it is critical to avoid fully enclosed voids, as they can make it impossible to remove the powder or support structures. To detect the presence of enclosed voids, image analysis is conducted on all 3D metamaterial units in the database. Metamaterial units with enclosed voids are categorized as 1 and those without enclosed voids are categorized as 0.

With the aforementioned manufacturability metrics, we evaluate the manufacturability of all samples in the 3D metamaterial unit database. The statistics of the manufacturability metric values are summarized in Fig. 2b and c.

3 Deep generative model-based design framework

This section introduces an integrated manufacturability-aware deep generative model for the optimal design of metamaterial units under manufacturing constraints. The proposed model is evaluated on two aspects: the reconstruction accuracy and the accuracy of predicting properties and manufacturability metrics values.

3.1 Overall design framework

The integrated manufacturability-aware deep generative model-based design framework consists of two major components:

(1) A manufacturability-aware deep generative model for low-dimensional representations of 3D metamaterial units and prediction of their corresponding properties. The low-dimensional representation is employed as the structure design space. The manufacturability-aware deep generative model consists of two parts: (a) a Variational Autoencoder (VAE) for feature learning, which learns parametric latent features from the high-dimensional 3D metamaterial image data through encoder and (b) supervised learning models that establish connections between the encoded latent vectors and the mechanical properties and manufacturability metrics. The supervised learning models also perform regularization on the latent feature space. Details of the model are introduced in Sect. 3.2.
(2) A design optimization approach for generating novel structures with desired properties and manufacturability by exploring the latent space. Genetic algorithm (NSGA-II) is employed in optimization due to its capability of overcoming local optima to obtain the global optimum. As the design properties and manufacturability are obtained using the trained supervised learning model during the optimization process, the computing efficiency is not a concern here. The design approach can be stated as follows:

$$\min_{z} \; [f_1(z), f_2(z) \ldots, f_{n_f}(z)]$$

$$s.t. c_j(z) \leq 0 \tag{3}$$

where z is a vector of design variables in the form of the latent variable vector learned from the deep generative model. $f_i (i = 1, 2, \ldots, n_f)$ are the objective functions related to the mechanical properties, $c_j (j = 1, 2, \ldots, n_c)$ are the constraint functions based on the manufacturability metrics. n_f

is the number of objective functions. n_c is the number of manufacturability constraints. f_i and c_j are functions of $\boldsymbol{z}$, as all supervised learning models of mechanical properties and manufacturability metric values take $\boldsymbol{z}$ as input. The objective functions of mechanical properties are normalized, so that the design framework is independent from the selection of base materials (Fig. 4).

3.2 Manufacturability-aware deep generative model for feature learning

VAE (Kingma and Welling 2014), originated from autoencoder, contains two components: encoder and decoder. The VAE's encoder conducts nonlinear dimensionality reduction and compresses the high-dimensional data ($\boldsymbol{x}$) into a low-dimensional latent space (z). The encoder can be expressed as $Q_\phi(z|\boldsymbol{x})$, which is the approximate posterior that follows a normal distribution and ϕ is the vector of the encoder parameters. The decoder, also a nonlinear operator, can map back the low-dimensional latent feature space to the original high-dimensional input data space. The decoder is expressed as $P_\theta(\boldsymbol{x}|z)P_\theta(z)$, where θ is the vector of decoder parameters. $P_\theta(z)$ is the prior distribution of latent variables and $P_\theta(\boldsymbol{x}|z)$ is the approximated distribution of $\boldsymbol{x}$ conditioned on z. The VAE embeds the Bayesian inference in the autoencoder architecture, which regularizes the latent feature space into a Gaussian distribution. The loss function of VAE includes two parts, and it can be expressed as follows:

$$L_{\mathrm{VAE}} = L_{(\boldsymbol{x},\hat{\boldsymbol{x}})} + L_{\mathrm{KL}}(z, N(0, \boldsymbol{I}_d)) \tag{4}$$

where z represents the latent vectors, $\boldsymbol{x}$ represents the input data, and $\hat{\boldsymbol{x}}$ represents the reconstruction data. $L_{(\boldsymbol{x},\hat{\boldsymbol{x}})}$ is the reconstruction loss, where $L_{(\boldsymbol{x},\hat{\boldsymbol{x}})} = \frac{1}{n}\sum_{i=1}^{n}(\boldsymbol{x}-\hat{\boldsymbol{x}})^2$, which is the mean squared error between the input data $\hat{\boldsymbol{x}}$ and the reconstruction data $\boldsymbol{x}$. n represents the number of training data in the VAE model. $L_{\mathrm{KL}}(z, N(0, \boldsymbol{I}_d))$ is the Kullback–Leibler divergence loss, which measures the differences

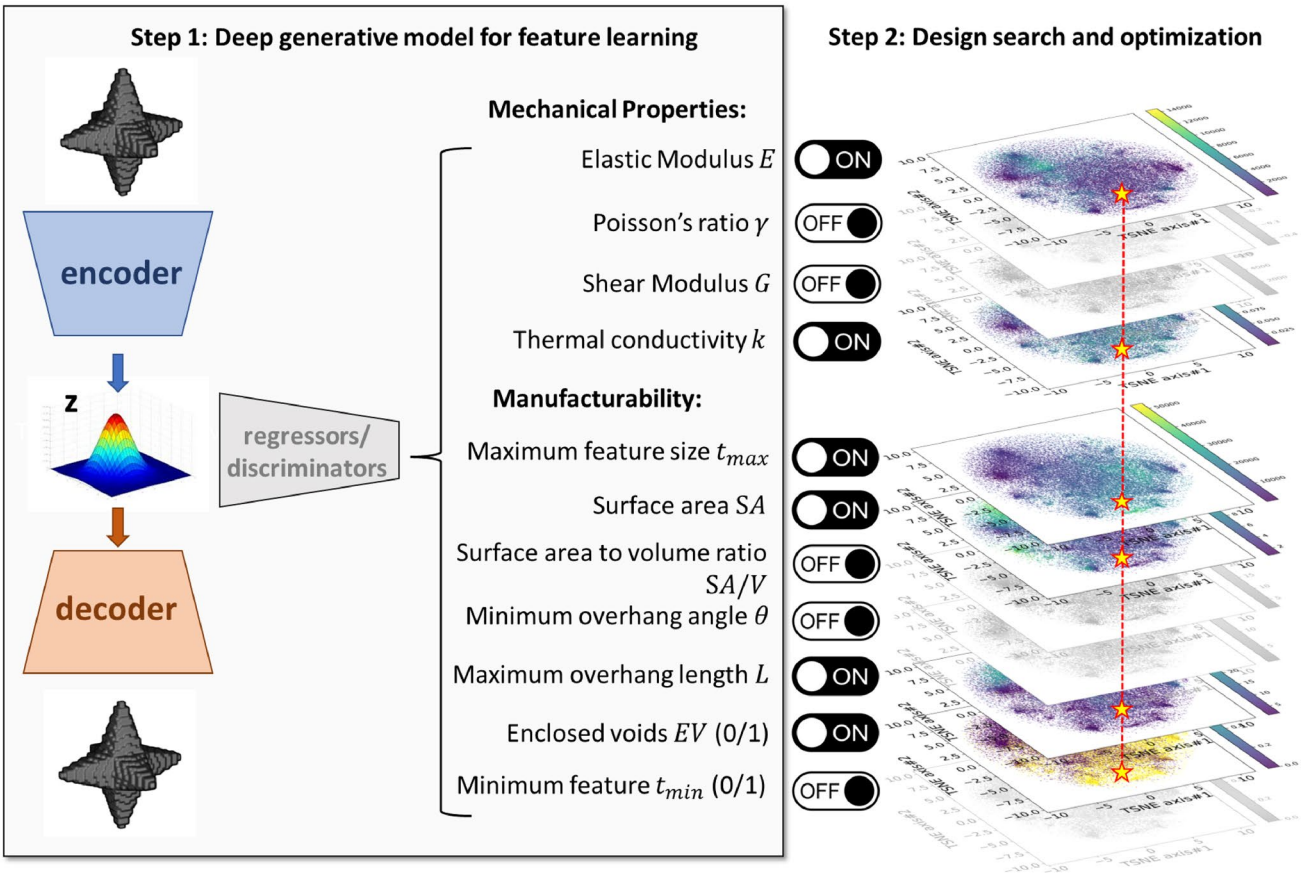

Fig. 4 Integrated manufacturability-aware deep generative model-based structure design framework. Step 1 is to create a deep generative model that embeds mechanical properties and manufacturability information in the latent space. Step 2 is to conduct design optimization guided by mechanical properties and manufacturability in the latent space. 2D tSNE representations of the latent space are provided. The colors in each plot represent different levels of mechanical properties and manufacturability metrics values. Each layer (objective or constraint function) can be turned on/off to meet various design requirements. The star and dashed line indicate the locations of one metamaterial design in the property/manufacturability metric spaces

between the distribution of latent vectors $\boldsymbol{z}$ and a normal distribution $N(0, \boldsymbol{I}_d)$.

Previous research studies (Li and Wang 2020; Xu et al. 2022) have shown that the latent feature space encoded by a stand-alone VAE only captures the geometrical information of the input data, thus hindering its ability to capture the structure–properties relationships. To address this limitation, we propose a manufacturability-aware deep generative model, where the supervised learning models are directly attached to the latent feature space encoded by VAE, to link the latent features to the mechanical properties and AM manufacturability metrics. The supervised learning models are trained simultaneously with the encoder and decoder during the training process. Supervised learning models of mechanical properties and the AM manufacturability metrics regularize the latent feature space to mitigate the overfitting issue. After the manufacturability-aware deep generative model is trained, the obtained latent feature space not only contains the samples' geometrical information but also contains the mechanical properties/manufacturability information learned from the supervised learning models. The proposed manufacturability-aware deep generative model outperforms the deep generative modeling approach that trains the VAE and the supervised learning models separately (Appendix A2).

The loss function of supervised learning models is defined as the sum of the mechanical properties losses (L_{Prop}) and the manufacturability metrics losses (L_{Manu}):

$$L_{surpervised} = L_{Prop} + L_{Manu} \tag{5}$$

Losses for the properties and manufacturability metrics are treated in two ways. For the continuous variables (e.g., surface area, maximum overhang length, minimum overhang angle, maximum feature size, elastic modulus, Poisson's ratio, and heat conductivity), a regressor is used to map the latent variables-properties relations; for discrete manufacturability metrics (e.g., existence of the enclosed voids and existence of unprintable features), discriminators are used to link them to the latent feature space. The regressors and discriminators are deep neural networks with fully connected layers, which map the latent features to the properties and manufacturability metrics. We use the mean squared error (MSE) loss L_{MSE} in the regressors, where $L_{MSE} = \frac{1}{n}\sum_{i=1}^{n}(Y_i - \widehat{Y}_i)^2$; we use the binary cross-entropy loss L_{BCE} in the discriminators, where $L_{\mathrm{BCE}} = -\frac{1}{n}\sum_{i=1}^{n}(Y_i \cdot log\widehat{Y}_i + (1 - Y_i)\cdot \log(1 - \widehat{Y}_i))$. $\widehat{Y}_i$ represents the true response of the i^{th} sample, Y_i represents the predicted response of the i^{th} sample and n represents the total number of sample points. Therefore, in this work, Eq. 5 can be further expressed as follows:

$$\begin{aligned} L_{surpervised} =& \frac{1}{n}\sum_{i=1}^{n}\left(E_i - \hat{E}_i\right)^2 + \frac{1}{n}\sum_{i=1}^{n}\left(\nu_i - \hat{\nu}_i\right)^2 + \frac{1}{n}\sum_{i=1}^{n}\left(G_i - \hat{G}_i\right)^2 \\ &+ \frac{1}{n}\sum_{i=1}^{n}\left(k_i - \hat{k}_i\right)^2 + \frac{1}{n}\sum_{i=1}^{n}\left(SA_i - \widehat{SA}_i\right)^2 \\ &+ \frac{1}{n}\sum_{i=1}^{n}\left(\frac{SA}{V}_i - \frac{\widehat{SA}}{V}_i\right)^2 + \frac{1}{n}\sum_{i=1}^{n}\left(L_i - \hat{L}_i\right)^2 \\ &+ \frac{1}{n}\sum_{i=1}^{n}\left(\theta_i - \hat{\theta}_i\right)^2 + \frac{1}{n}\sum_{i=1}^{n}(t_{max_i} - (\widehat{t_{max_i}})^2 \\ &- \frac{1}{n}\sum_{(i=1)}^{n}(t_{min_i}\cdot \log \widehat{t_{\min_i}}) + (1 - t_{min_i})\cdot \log(1 - \widehat{t_{\min_i}})) \\ &- \frac{1}{n}\sum_{i=1}^{n}(EV_i \cdot \log \widehat{EV_i}) + (1 - EV_i)\cdot \log(1 - \widehat{EV_i})) \end{aligned} \tag{6}$$

As this work focuses on designing symmetric metamaterial units, the loss for enhancing geometrical symmetricity $L_{\mathrm{symmetric}}$ of the reconstructed metamaterial units is defined as follows:

$$L_{\mathrm{symmetric}} = \sum_{i=1}^{l}\sum_{j=1}^{l}\sum_{k=1}^{l}\left(\sum_{\mathrm{axis}=0,1,2}\left|\boldsymbol{x}_{ijk} - \boldsymbol{x}_{ijk}^{\mathrm{T}_{\mathrm{axis}}}\right|\right) \tag{7}$$

where $\boldsymbol{x}^{\mathrm{T}_{\mathrm{axis}}}$ represents the transposed structure of the reconstructed structure $\boldsymbol{x}$ along three different axes (refer to axis 0, 1, and 2 in Fig. 5). l represents the length of the structures, where $l = 48$ in our dataset. The difference between the transposed reconstruction structure $\boldsymbol{x}^{\mathrm{T}_{axis}}$ and the reconstruction structure $\boldsymbol{x}$ is used as the loss function for geometrical symmetry, which is calculated as the sum of absolute error between each voxel.

When arranging the reconstructed metamaterial units into grids to create a bulk material, it is crucial to ensure that the units can connect seamlessly at the boundaries while maintaining connectivity within each unit. A connectivity loss $L_{\mathrm{connectivity}}$ is defined for this purpose. The reconstructed structure $\boldsymbol{x}$ is first copied along axis 0, 1, and 2 each with 3 times to construct structure $\boldsymbol{X}$ of 3×3 units. $\boldsymbol{X}$ is a binary matrix, in which the solid phase is represented by 1 and the pore phase is represented by 0. Image analysis is conducted to check the 26 connectivity of the solid phase. If the units are connected seamlessly at the boundaries and internally, the number of isolated parts nip should be 1. Therefore, the loss term that enhances connectivity of the reconstructed metamaterial units is defined in Eq. 8 as follows:

$$L_{\mathrm{connectivity}} = \mathrm{nip}(\boldsymbol{X}) - 1 \tag{8}$$

To sum up, the final loss function of the proposed deep generative model consists of four parts: loss for training the variational autoencoder, loss for training supervised learning models, loss of geometrical symmetric, and loss for ensuring connectivity at the boundaries:

$$L_{\mathrm{total}} = \alpha_1 L_{\mathrm{VAE}} + \alpha_2 L_{\mathrm{supervised}} + \alpha_3 L_{\mathrm{symmetric}} + \alpha_4 L_{\mathrm{connectivity}} \tag{9}$$

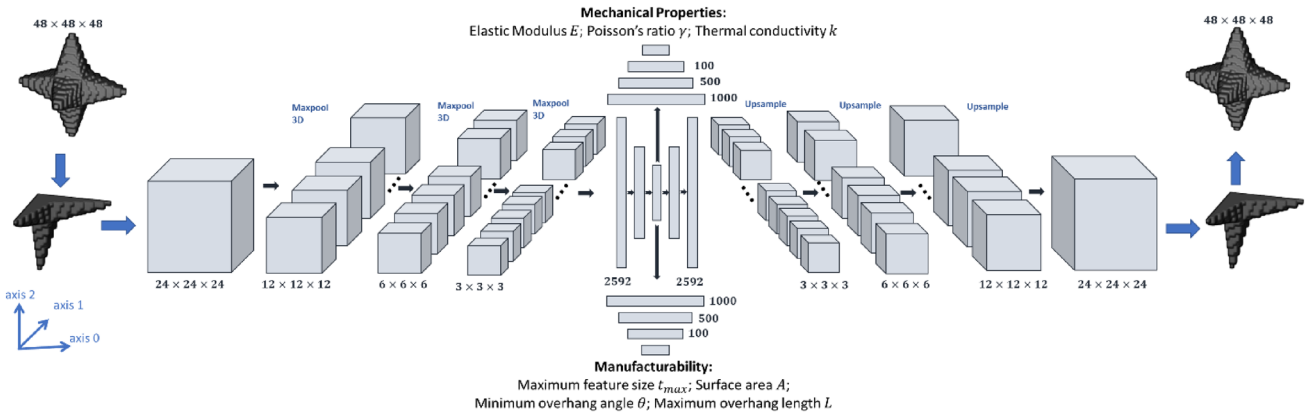

Fig. 5 Detailed architecture of the manufacturability-aware deep generative model

α_1, α_2, α_3, and α_4 are the weights to balance different parts of loss terms. Based on our experimental tests, $\alpha_1 = 5$, $\alpha_2 = 1$, $\alpha_3 = 0.01$, and $\alpha_4 = 0.01$ are used in this study. To achieve a balance between the accuracies of the deep generative model and the dimensionality of the latent feature space, we conducted a convergence study, based on which the dimensionality of the latent space is set as 100 (Appendix A3). The detailed architecture of the manufacturability-aware deep generative model is shown in Fig. 5. Hyperparameters of this model are listed in Appendix A4.

The 3D metamaterial unit dataset is divided into two sets, 39,378 (90%) for training and 4375 (10%) for testing. The 3D metamaterial units are structural symmetrical structures with the shape of $48 \times 48 \times 48$ voxels. To alleviate the computational cost while training the deep generative model, we leverage the geometrical symmetry of the metamaterial designs and only use one-eighth of the structure as the input. Therefore, the input data has a dimension of $24 \times 24 \times 24$ voxels. The reconstructed data would be mirrored three times to obtain the original $48 \times 48 \times 48$ voxels shape. The proposed deep learning model is implemented in PyTorch (Paszke et al. 2019). Adam is used as the optimizer for parameter optimization. The number of epochs is set to 400.

3.3 Validation of the manufacturability-aware deep generative model

Here, the proposed manufacturability-aware deep generative model is validated in two aspects: the reconstruction accuracy of the VAE component and the property/manufacturability prediction accuracies the regressors and discriminators.

The reconstruction accuracy is evaluated by performing a voxel-to-voxel comparison of the original structure image input to the encoder and the structure reconstructed by the decoder. A few examples are shown in Fig. 6. The metric of reconstruction accuracy is defined as follows:

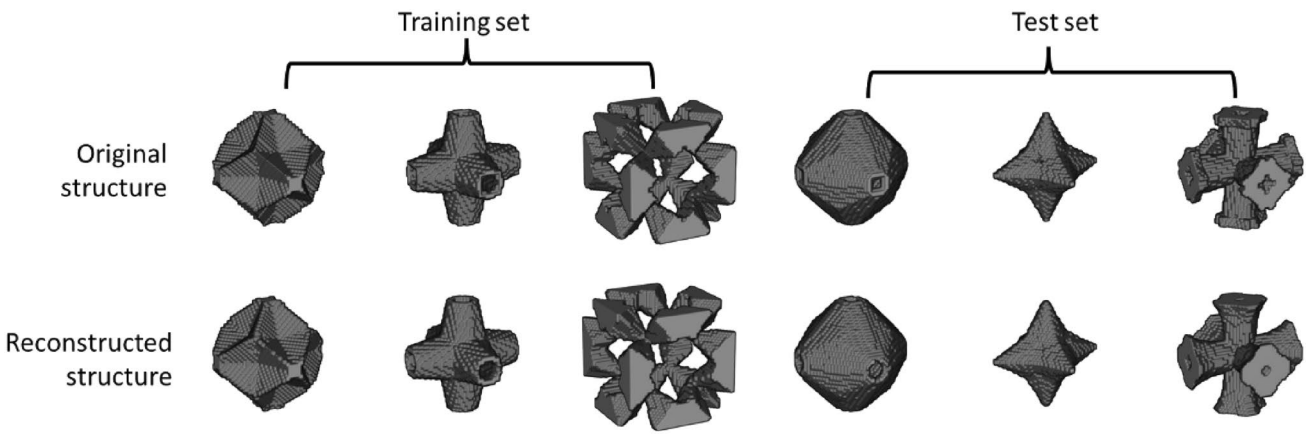

Fig. 6 Original and reconstructed structures from the training set and the test set

Table 1 Prediction accuracies of the supervised learning models

	Reconstruction accuracy	Property			
		k	E	G	ν
Training set	0.9726	0.9611	0.9740	0.9750	0.9561
Testing set	0.9725	0.9477	0.9631	0.9651	0.9278

	Manufacturability						
	SA	SA/V	$t_{\max}$	L	θ	$t_{\min}$	EV
Training set	0.9805	0.9772	0.9831	0.9025	0.8704	0.8569	0.9627
Testing set	0.9787	0.9726	0.9819	0.87523	0.8400	0.8200	0.9425

Please refer to Eq. 11 for the accuracy metrics of calculating SA, SA/V, $t_{\max,\,\mathrm{L}}$, θ, k, E, G, and ν and refer to Eq. 12 for the accuracy metrics of calculating $t_{\min}$ and EV

$$Accuracy_{\text{reconstruction}} = 1 - \frac{1}{N}\frac{1}{l^3}\sum_{i=1}^{l}\sum_{j=1}^{l}\sum_{k=1}^{l}\left|O_{ijk} - R_{ijk}\right| \quad (10)$$

where N represents the total amount of test structures used and l represents the voxel length of the structures, where $l = 48$ in our dataset. In the first set, the trained models are employed to reconstruct the images in the training set to verify the accuracy of the training process. In the second set, the trained models are employed to reconstruct the images in the test set. The reconstruction accuracies of the training and test sets are presented in Table 1. The accuracies are above 0.972, which means the average number of mismatched voxels in one of the metamaterial unit is within 2.8% of the total number of voxels ($48 \times 48 \times 48$).

The coefficient of determination (R^2) is used to evaluate the accuracies of the regressors, which quantifies the deviation of data from their true mean value:

$$R^2 = 1 - \frac{\sum\left(Y_i - \hat{Y}_i\right)^2}{\sum\left(Y_i - \overline{Y_i}\right)^2} \quad (11)$$

where Y_i represents the true response of the i^{th} sample, $\hat{Y}_i$ represents the predicted response of the i^{th} sample, and n_{sample} represents the total number of sample points. $\overline{Y_i}$ is the averaged value of $Y_{i(true)}$ and $\overline{Y_i} = \frac{1}{n_{\text{sample}}}\sum Y_i$. A higher R^2 value means a more accurate model. The values predicted by the regressors versus the ground truth values are shown in Fig. 7.

The accuracy metrics of the discriminators are defined as the ratio of the number of correct predictions to the total number of predictions. For binary classification, it is expressed as follows:

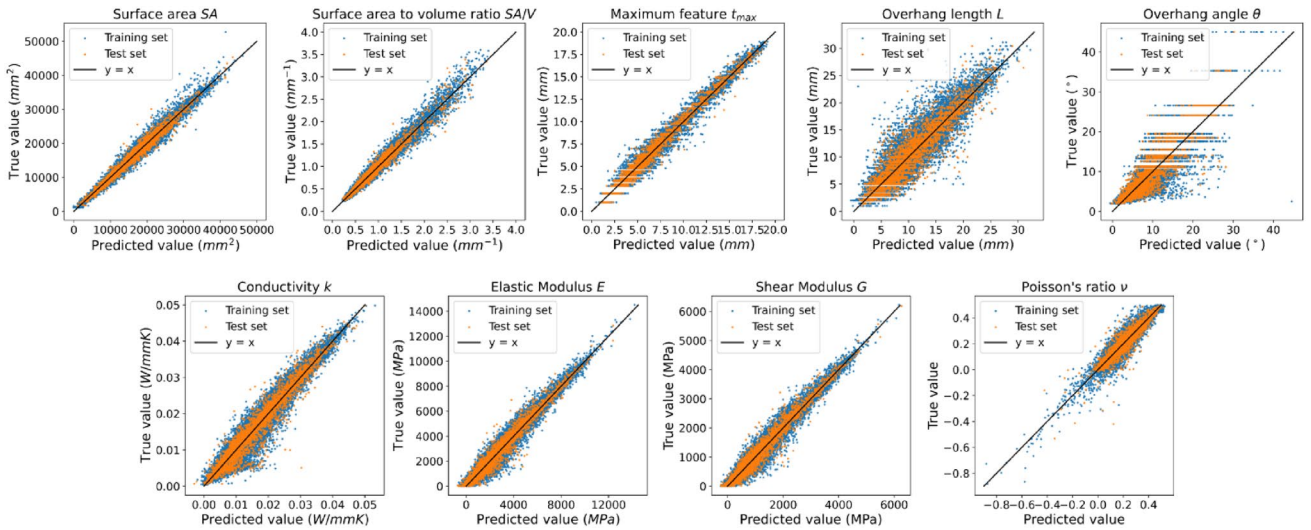

Fig. 7 Predicted values vs ground truth values of the regressors for predicting continuous manufacturability metrics and mechanical properties

$$Accuracy_{\mathrm{BCE}} = \frac{\mathrm{TP} + \mathrm{TN}}{\mathrm{TP} + \mathrm{TN} + \mathrm{FP} + \mathrm{FN}} \tag{12}$$

where TP represents true positives, TN represents true negatives, FP represents false positives, and FN represents false negatives. As shown in Table 1, both regression models and classification models were able to achieve satisfactory accuracies.

4 Metamaterial design cases

4.1 Generation of new metamaterial units by unsupervised generative design

We firstly present a case to illustrate the mechanism of generating continuously evolving metamaterial unit designs by manipulating the values of the latent variables. The basic idea is to morph the metamaterial unit designs by manipulating the values of the latent variables.

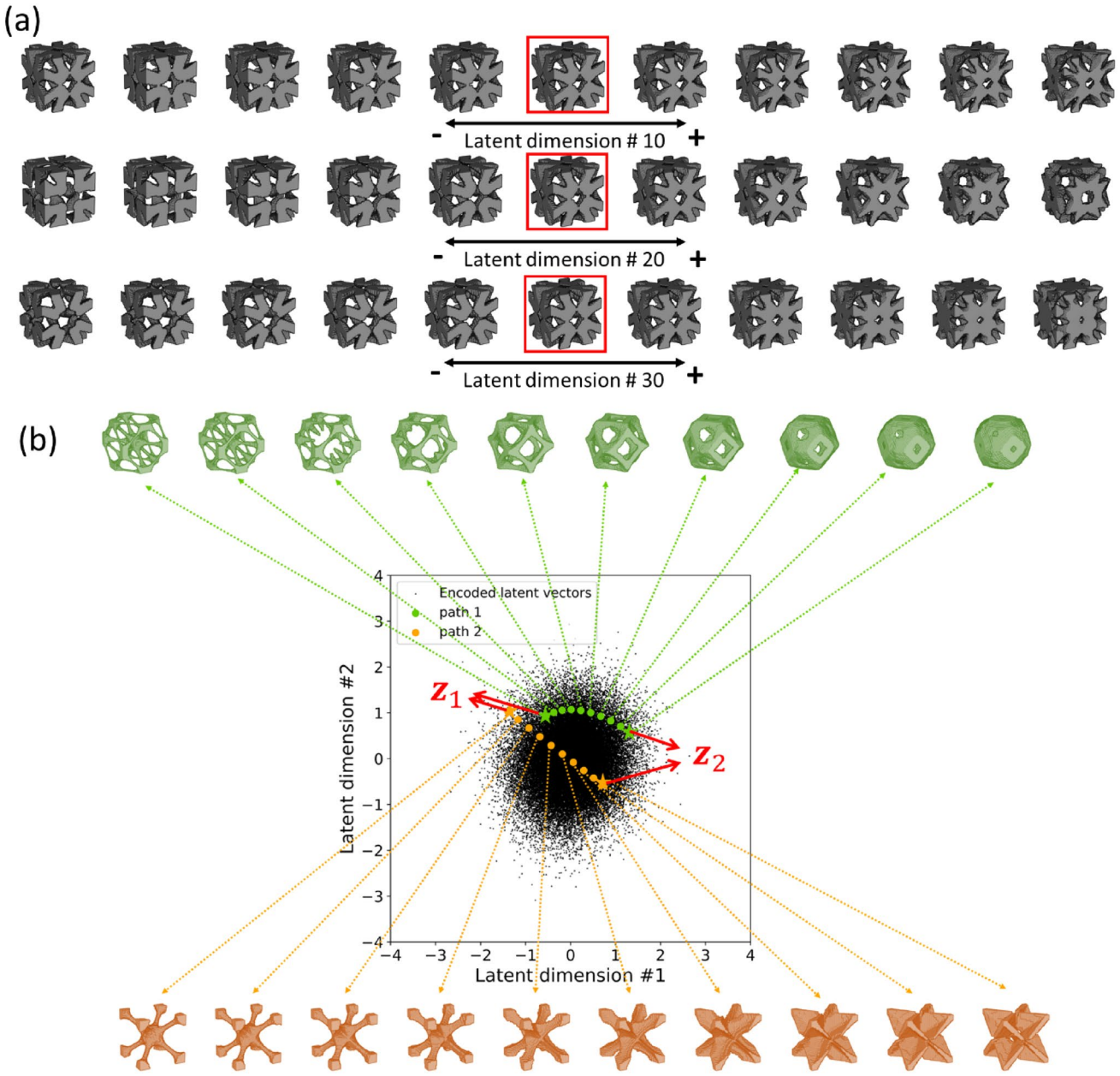

Fig. 8 **a** Generating metamaterial units by manipulating the values of one latent variable and fixing others. **b** Two examples of generating continuously evolving metamaterial designs by spherical linear interpolation in the latent space

We first randomly choose a metamaterial unit and vary one of its corresponding latent variables along negative and positive direction. When we vary one latent variable, the others remain to its original values. The resultant generated metamaterial units are shown in Fig. 8a. We only show the shape transient by modifying latent variable values on three randomly selected latent dimensions.

Second, we demonstrate the generative design capability by conducting the interpolation between two existing samples. Linear interpolation has been traditionally used because of its simplicity. However, for a high-dimensional latent space with a Gaussian prior, linear interpolation can cause the generated shapes to become blurry due to deviating from the model's prior distribution. Therefore, spherical linear interpolation, which is firstly introduced and implemented in White (2016), is employed to interpolate between two points in the latent space. By avoiding sampling from locations that are highly unlikely given the model's prior distribution, spherical linear interpolation provides a more appropriate method for generating shapes. The spherical linear interpolation is formulated as follows:

$$z_\mu = slerp(z_1, z_2; \mu) = \frac{\sin(1-\mu)\theta}{sin\theta} z_1 + \frac{\sin\mu\theta}{sin\theta} z_2 \tag{13}$$

where slerp represents the spherical linear interpolation that treats the interpolation as a great circular path on a n-dimensional hypersphere; z_1, z_2 are two randomly selected latent vectors on the latent feature space; and μ represents the location along the path, with the start and end points marked as 0 and 1, respectively. Thus, $0 \le \mu \le 1$; θ represents the angle subtended by the arc, so that $\cos\theta = z_1 \cdot z_2$. Two examples of generative metamaterial design by spherical linear interpolation in latent space are shown in Fig. 8b. In each example, we randomly choose two 3D metamaterial units from the training dataset. The two metamaterial units are encoded to obtain the corresponding latent vectors z_1, z_2. The spherical linear interpolation is carried out between these two latent vectors. A total of eight designs are generated along the path, corresponding to μ values of 0, $\frac{1}{9}$, $\frac{2}{9}$, $\frac{1}{3}$, $\frac{4}{9}$, $\frac{5}{9}$, $\frac{2}{3}$, $\frac{7}{9}$, $\frac{8}{9}$, and 1. To aid visualization, we plotted the two interpolation paths in two randomly selected latent dimensions.

4.2 Design optimization: designing metamaterial unit with negative Poisson's ratio under manufacturability constraints

The Poisson's ratio defines the ratio between the transverse strain and axial strain. Materials that are uniaxially compressed are typically expanded in the orthogonal directions to the applied load. Conversely, materials with negative Poisson's ratio contract in the transverse direction under applied load. Metamaterials with the auxetic behavior have a great potential in the development of protective objects with higher indentation resistance, such as shock absorbers, packing material, and body armors (Babaee et al. 2013; Evans 1991; Grima et al. 2015; Yasuda and Yang 2015).

In this design case, the objective is to create metamaterial units with negative Poisson's ratio and a good additive manufacturability. The design problem is formulated as minimizing the Poisson's ration under the following AM manufacturability constraints: the maximum feature size $t_{\max}$ should not exceed 5 mm, the surface area-to-volume ratio should not exceed 1 mm^{-1}, all the small features can be printed, and the connectivity is ensured at the metamaterial unit boundaries ($L_{\text{connectivity}} = 0$). The problem statement is expressed as follows:

$$\begin{aligned}
&\min_{z} \ \nu(z) \\
&\text{s.t.} \quad t_{\max}(z) - 5 \le 0 \\
&SA/V(z) - 1 \le 0 \\
&\nu(z) < 0 \\
&t_{\min}(z) = 0 \\
&L_{\text{connectivity}}(z) = 0 \\
&min(z) \le z \le max(z)
\end{aligned} \tag{14}$$

As discussed in Sect. 3.1, we employ NSGA-II to search for the optimal design represented in the form of a latent vector z. Subsequently, the optimal latent vector is decoded to obtain the metamaterial unit in the format of a 3D voxel image. The design optimization process is repeated three times independently with different initial points and seeds in the optimization process. Three different optimal designs are obtained, as shown in Fig. 9. The Poisson's ratios of each of the three optimal designs are verified using finite element simulation in ABAQUS and their AM manufacturability metric values are verified through voxel-based image

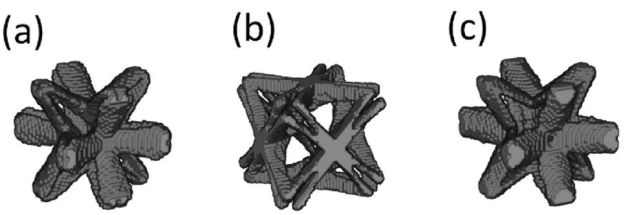

Fig. 9 Three optimal design candidates found by the proposed approach

Table 2 Predicted and ground truth Poisson's ratio of 3D metamaterial optimal design candidates and their manufacturability

Design candidates		Objective		Manufacturability metrics							
		Poisson's ratio ν		$\frac{SA}{V}\,(\mathrm{mm}^{-1})$		$t_{\max}(\,\mathrm{mm}\,)$		$t_{\min}$		$L_{\text{connectivity}}$	
Constraints		–		1		5		0		0	
	P	T	P	T	P	T	P	T	P	T	
(a)	− 0.301	− 0.297	0.97	0.989	3.10	3.04	0	0	0	0	
(b)	− 0.483	− 0.506	0.98	1.116	4.85	5	0	0	0	0	
(c)	− 0.401	− 0.381	0.99	0.998	4.20	4.24	0	0	0	0	

P represents the predicted values and T represents the ground truth values

analysis and are shown in Table 2. The optimal designs obtained exhibit exceptional mechanical properties, ranking among the top 0.1% in the metamaterial database in terms of Poisson's ratio. Only 48 out of 46,840 metamaterial units in the existing database have slightly smaller negative Poisson's ratios. Notably, two out of the three obtained designs meet all manufacturability constraints, while design (b) exceeding the present surface area limit within 12%. By contrast, the 48 metamaterial units with smaller negative Poisson's ratio than the obtained optimal designs in the database do not meet the manufacturability constraints.

4.3 Design optimization: designing metamaterial units with maximized bulk modulus under manufacturability constraints

In this design case, the objective is to generate a 3D metamaterial unit with a maximized bulk modulus (B), while ensuring there are no enclosed voids and the structure is within a specific volume fraction range. The optimal design found by our approach is compared with the metamaterial unit designs obtained by the method proposed in literature (Takezawa et al. 2017), where a TO method is proposed for the design of maximized bulk modulus metamaterial units without enclosed voids. To ensure a fair comparison, the same volume fraction value 0.3 is used in the comparative study. Bulk modulus of a metamaterial unit can be obtained by Eq. 15, where E and ν can be obtained by supervised learning model. The bulk modulus is normalized.

$$B = \frac{E}{3(1-2\nu)} \tag{15}$$

In this design case, the manufacturability metrics take the same settings used in literature (Takezawa et al. 2017): there should not exist any enclosed voids in the structure. In addition, the structural connectivity at the boundaries of the metamaterial units is also considered in our design search process. The formulation of the problem is then stated as following:

$$\begin{aligned} &\max_{z} \; B(z) \\ &\text{s.t. } \mathrm{EV}(z) = 0 \\ &L_{\text{connectivity}}(z) = 0 \\ &|VF(z) - 0.3| = 0.001 \\ &\min(z) \le z \le \max(z) \end{aligned} \tag{16}$$

where z represents a vector of latent variables. VF(·) represents the volume fraction of the decoded 3D metamaterial unit, which can be seen as a function of z. To ensure a fair comparison, we used a hollow tetradecahedron

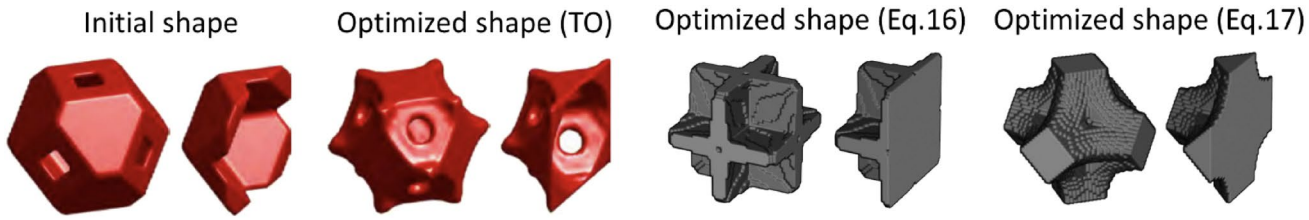

Fig. 10 **a** Initial shape for design search. **b** Optimal design with vf = 0.3 from TO method. **c** Optimal design by the proposed method with consideration of the same manufacturability constraints (Eq. 16). **d** Optimal design by the proposed method with consideration of an augmented set of manufacturability constraints (Eq. 17)

Table 3 Comparison of the metamaterial unit designs obtained by the proposed framework and the optimal design reported in literature

Design formulation in Eq. 16	Objective		Manufacturability							
	B(Normalized)		$A\left(mm^2\right)$		$L(\text{mm})$		$\theta(^\circ)$		$t_{\min}$	
Constraints	–	–	–		–		–		0	0
	P	T	P	T	P	T	P	T		
TO-(Takezawa et al. 2017)	–	0.102	0	0	0	0				
Proposed approach	0.131	0.120	0	0	0	0				

Design formulation in Eq. 17 (more constraints)	Objective		Manufacturability											
	B(Normalized)		$\frac{SA}{V}\left(\text{mm}^{-1}\right)$		$L(\text{mm})$		$\theta(^\circ)$		$t_{\min}$		EV		$L_{\text{connectivity}}$	
Constraints	–	–	≤ 0.5		≤ 10		≥ 10		0		0		0	
	P	T	P	T	P	T	P	T	P	T	P	T	P	T
Proposed approach	0.091	0.074	0.31	0.305	4.8	5	15.2	11.38	0	0	0	0	0	0

P represents predicted values and T represents ground truth values

geometry, which is similar to the initial shape in Fig. 10a, as the starting point for the design search. NSGA-II is applied to search for the optimal design represented in the form of a latent vector z. Subsequently, the optimal latent vector is decoded to obtain the metamaterial unit in the format of a 3D voxel image (Fig. 10c). The predicted performance and true performance of the optimal design are compared and shown in Table 3. The proposed framework was able to generate an optimal design that exhibits a higher normalized bulk modulus when compared to the design reported in Takezawa et al. (2017).

In addition, the proposed design framework offers the flexibility to incorporate more manufacturability metrics for the same design objective. We conducted another case study by setting the manufacturability constraints as follows: the maximum overhang length should not exceed 10 mm, the overhang angle θ should not less than 10°, the surface area-to-volume ratio should not exceed 0.5 mm^{-1}, and there should not exist any enclosed voids or unprintable small features. Also, the connectivity at the boundaries of the metamaterial units should be ensured. Thus, the formulation of the problem is stated as following:

$$\max_{z} B(z)$$

$$s.t. L(z) - 10 \leq 0$$

$$-\theta(z) + 10^\circ \leq 0$$

$$SA/V(z) - 0.5 \leq 0$$

$$EV(z) = 0$$

$$t_{\min}(z) = 0$$

$$L_{\text{connectivity}}(z) = 0$$

$$|VF(z) - 0.3| = 0.001$$

$$min(z) \leq z \leq max(z) \tag{17}$$

The optimal design under the aforementioned manufacturability constraints is shown in Fig. 10d. The performance and the manufacturability metrics values of the optimal design are listed in Table 3. Compared to the optimal designs produced by TO (Takezawa et al. 2017), the design obtained using the proposed approach has relatively lower modulus, but satisfying more manufacturability constraints. Based on the results, we conclude a few strengths and limitations of the proposed approach:

- The deep generative model-based approach has the capacity to explicitly incorporate multiple manufacturability constraints within the problem formulation, while Takezawa et al. (2017) meets the no-enclosed-void constraint by restricting the design domain.
- TO is sensitive to the initial condition, whereas the proposed approach has the capability of overcoming the local minima in design search.
- TO is based on the gradient-based search, which is more efficient in convergence; the proposed method uses non-gradient-based optimization algorithm, which requires a large number of generations. It is to be noted that the design performances are obtained by the trained supervised learning models, thus the computing time is not a major concern in this work.

- TO method enables property-driven freeform design; our proposed method is confined to the design space learned from the training database.

4.4 Multi-objective design optimization: designing metamaterial with maximized elastic modulus and minimized heat conductivity under manufacturability constraints

In this case, we present a multi-objective design of metamaterial units for maximum elastic modulus and minimum heat conductivity, all while adhering to additive manufacturability constraints. Metamaterials with high elastic modulus and low heat conductivity offer enhanced resistance to deformation and effective heat control. These materials find applications in aerospace components, energy storage devices, biomedical implants, and more. To showcase the capacity of our proposed design framework to handle multiple manufacturability constraints, we activate all the constraints that were previously integrated into the deep generative model.

A multi-objective design optimization is conducted to maximize the elastic modulus (E) and minimize the heat conductivity (k) of the 3D metamaterial units. In this design case, the following manufacturability constraints are considered: the total surface area should not surpass 12,000 mm^2, the surface area-to-volume ratio should not surpass 0.5 mm^{-1}, the maximum overhang length should not exceed 10 mm, the overhang angle θ should not be less than 10°, the maximum feature size should not exceed 20 mm, the structure should not contain any enclosed voids, and the geometry connectivity at the metamaterial unit boundaries should be ensured. The design problem is formulated as follows:

$$
\begin{cases} \max\limits_{z} E(z) \\ \min\limits_{z} k(z) \end{cases}
$$

$$
\begin{aligned}
& s.t. SA(z) - 12000 \leq 0 \\
& SA/V(z) - 0.5 \leq 0 \\
& L(z) - 10 \leq 0 \\
& -\theta(z) + 10^\circ \leq 0 \\
& t_{\max}(z) - 20 \leq 0 \\
& EV(z) = 0 \\
& L_{\text{connectivity}}(z) = 0 \\
& \min(z) \leq z \leq \max(z)
\end{aligned} \tag{18}
$$

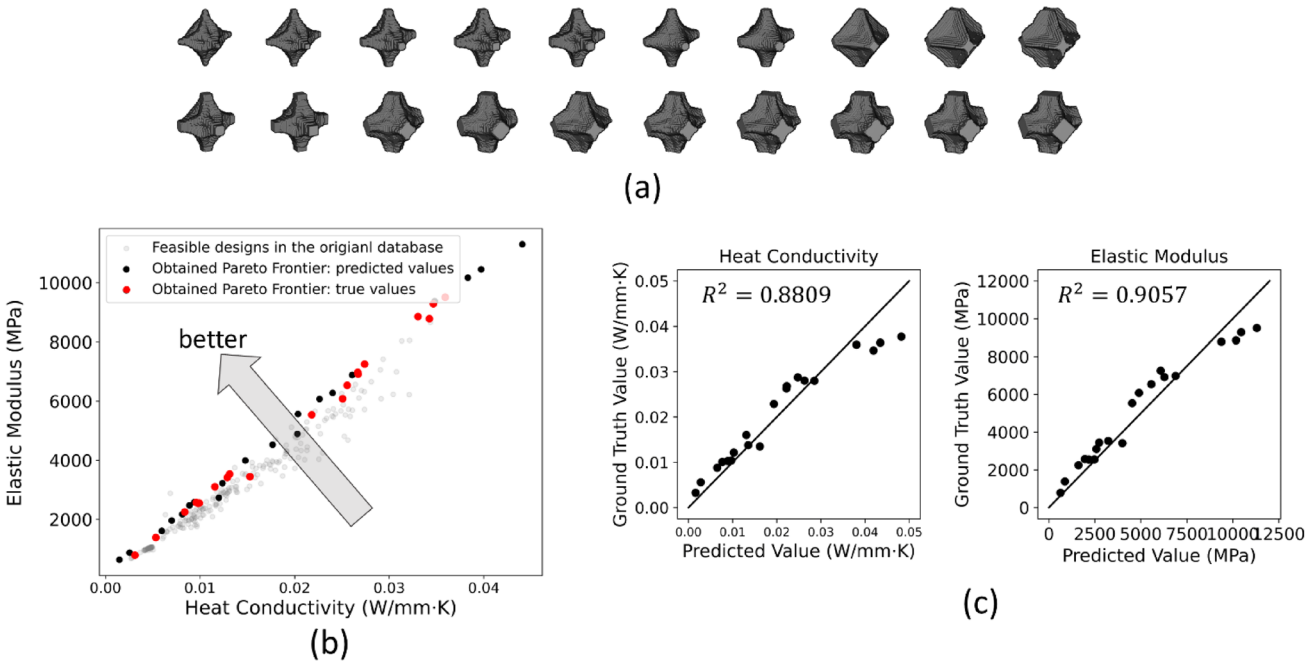

Fig. 11 **a** Non-dominated design set obtained by multi-objective optimization. **b** True heat conductivity and elastic modulus values obtained by finite element simulation and the predicted values by the supervised learning model. **c** Obtained designs: 3D metamaterial units with high elastic modulus and low thermal conductivity while satisfying the given manufacturability constraints

NSGA-II is applied to search for the optimal designs (on the Pareto frontier) represented in the form of a latent vector **z**. Subsequently, the optimal latent vector is decoded to obtain the metamaterial unit in the format of a 3D voxel image (Fig. 11a). As shown in Fig. 11b, the proposed design framework successfully generates designs that exceed the feasible designs in the original database in both stiffness and heat conductivity, while meeting manufacturability constraints. The true properties of the found designs are verified by simulations and their manufacturability is evaluated using image analysis. The predicted values and the corresponding ground truth values are compared in Fig. 11c. The predicted manufacturability constraints values and the ground truth manufacturability values are listed and compared in Appendix A5. 13 out of 20 optimal design candidates meet all manufacturability constraints. 35% optimal design candidates violate the maximum overhang angle constraint, with relative error within 46.5%. These violations are attributed to the prediction errors of the supervised learning models, which can be potentially mitigated by refining the model with more training data points. Notably, the overhang angle constraint is particularly prone to be violated due to its lower accuracy as compared to the other regression models (Table 1).

5 Conclusion

In this work, a manufacturability-aware deep generative model-based design framework is established for designing 3D metamaterial units for mechanical properties under AM manufacturability constraints. By leveraging the latent space learned by the deep generative model, the proposed framework enables both generative design and exploitative optimization. Our major conclusions are summarized as follows:

(1) The proposed design framework based on a manufacturability-aware deep generative model can learn a unified feature space that incorporates geometrical, manufacturability, and mechanical properties information. This feature space enables property-driven structure design with consideration of manufacturability constraints.
(2) The effectiveness of the proposed framework is demonstrated through three engineering case studies with different design objectives and manufacturability constraints.
(3) The proposed design framework offers flexibility in accommodating various mechanical properties and manufacturability constraints. Design objectives and manufacturability constraints can be easily turned on/off to meet various design requirements.
(4) In comparison to the gradient-based TO method, the proposed design framework generates optimal designs that are less sensitive to the choice of initial design. Moreover, it is capable of generating a diverse range of new designs that meet the specified design objectives and constraints.

In our future work, we plan to address the limitations of the proposed framework, which can be summarized as follows:

(1) Some discrepancies exist between the predicted responses and true responses for optimal designs, which are caused by the errors of the supervised learning models, particularly when the new designs require extrapolation in the latent space.
(2) We aim to expand the set of manufacturability metrics to enhance the generalizability of the proposed framework for a broader range of AM techniques.

Appendix

Details of the microstructure family template-based method

This method is used to generate the first group of microstructure samples in the database. This method is a four-step process:

Step 1: Define rectangular bars in the continuous cubic spatial domain $[0, l]^3$, where l represents the length of the spatial domain. The rectangular bars are defined by the coordinates of the pair of reference points $[loc_i, loc_j]=[(locx_i, locy_i, locz_i), (locx_j, locy_j, locz_j)]$ and the side length of the square cross-section of the bar (h). Therefore, each bar corresponds to 7 design variables. To avoid overly complicated structures, we only create 1 or 2 bars in this step.

Step 2: Voxelate the spatial domain $[0, l]^3$. In this work, we use $l = 48$, resulting in a $48 \times 48 \times 48$ voxel domain. The bars created in Step 1 are also voxelated. The voxels of the rectangular bars are referred as "original bar voxels" in the following steps.

Step 3: Map the original bar voxels by the midpoint of the grid along each axis sequentially, following the relationship $loc' = l - loc$. Through this mirroring process, the original bar voxels on one side of each axis's midpoint are reflected to the opposite side, creating a symmetric arrangement in all three directions.

Step 4: Record the indices of each voxel to enforce a hierarchical relationship between $locx_i, locy_i, andlocz_i$ coordinates. This step map the bar voxels $(locx_i, locy_i, locz_i)$ obtained by previous step to new locations

$(locx_i', locy_i', locz_i')$ by permuting their coordinates while adhering to the relationship $locx_i' > locy_i' > locz_i'$. This step enforces a cubic symmetry in the structure.

After completing the abovementioned steps, the rectangular bars defined within the spatial domain $[0, l]^3$ are mirrored to form a voxelated, cubic, symmetric metamaterial unit. For the metamaterial units generated by 1 bar, there are 7 design variables; for the metamaterial units generated by 2 bars, there are in total 14 design variables. Latin hyper sampling (LHS) is used to assign values to the parameters of each bar. In our LHS table, the values regarding the coordinates $(locx_i, locy_i, locz_i, locx_j, locy_j, locz_j)$ are generated in the range of $[0, l]$ and the parameter of side length h is generated in the range of $(0, l]$ (Fig. 12).

Deep generative model that trains VAE and supervised learning model separately

Here, we present an alternative modeling approach that trains the VAE and supervised learning models separately. The VAE is firstly trained to obtain a low-dimensional latent feature space that solely depends on the geometries of the 3D metamaterial units. Then, we use supervised learning models to establish the relationship between the latent feature variables and the mechanical properties and manufacturability metric values. The accuracy of this model is evaluated based on the reconstruction accuracy and the accuracies of the supervised learning models. The metrics are introduced in Eqs. 10–12. The results are presented in Table 4. Compared to the proposed integrated manufacturability-aware model (Table 1), the strategy of training the VAE and the supervised learning models separately show slightly higher accuracy in structural reconstruction but lower accuracies in

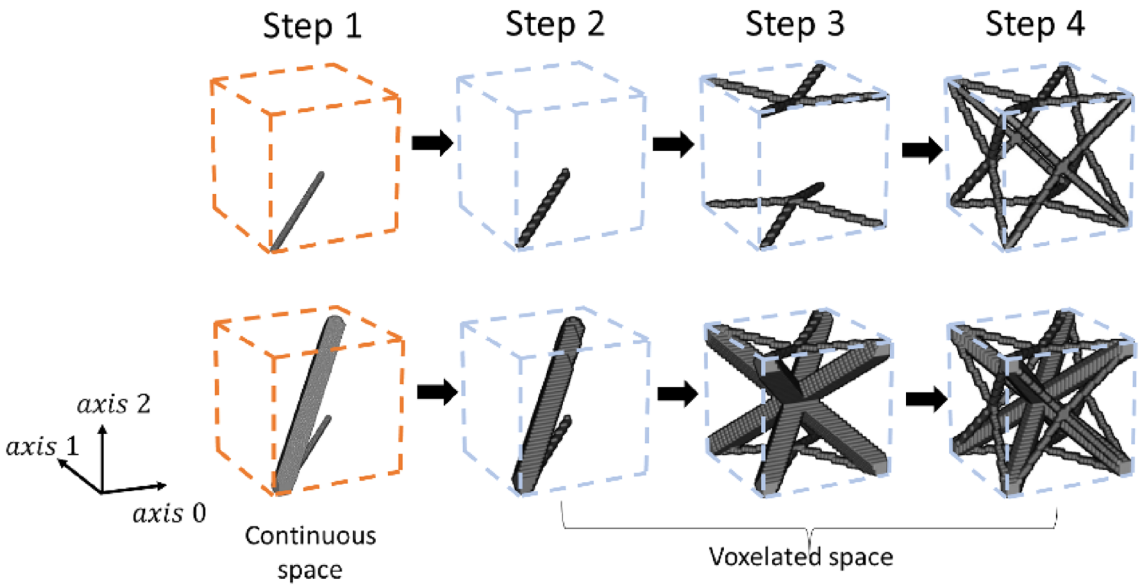

Fig. 12 Detailed generation process of the first metamaterial unit database

Table 4 Accuracies of the alternative modeling approach on reconstruction of 3D metamaterial units and prediction of properties and manufacturability metric values

	Reconstruction accuracy	Property			
		k	E	G	γ
Training set	0.9778	0.9172	0.9387	0.9288	0.9032
Testing set	0.9776	0.9067	0.9320	0.9256	0.8929

	Manufacturability						
	SA	SA/V	t_{max}	L	θ	t_{min}	EV
Training set	0.9594	0.9266	0.9472	0.8429	0.8076	0.8179	0.9211
Testing set	0.9566	0.9263	0.9456	0.8283	0.8042	0.8082	0.9122

predicting properties and manufacturability metric values. The lower prediction accuracies may lead to infeasible or low-performance designs found by optimization.

Convergence test to determine the dimensions of latent feature space

See Table 5.

Table 5 A convergence test to show the loss values of the proposed manufacturability-aware deep generative model on the test dataset

Latent dimension	$L_{(x,\hat{x})}$	L_{KL}	$L_{\mathrm{supervised}}$	$L_{\mathrm{symmetric}}$	$L_{\mathrm{connectivity}}$
25	0.0815	0.0474	0.0014	0.0016	0.0003
50	0.0732	0.0402	0.0014	0.0014	0.0003
75	0.0596	0.0316	0.0013	0.0013	0.0002
100	0.0584	0.0302	0.0012	0.0013	0.0002
125	0.0581	0.0290	0.0012	0.0013	0.0002
150	0.0580	0.0283	0.0012	0.0013	0.0002

All these models are trained using the same training strategies and sharing the same architecture except for the number of latent dimensions.

Hyperparameters of the manufacturability-aware deep generative model

See Table 6

Table 6 The detailed structure of the proposed manufacturability-aware deep generative model

Block	Specifications
Encoder	
Encoder Conv3d-1	(Conv32 + ReLU) × 3 + MaxPooling
Encoder Conv3d-2	(Conv64 + ReLU) × 3 + MaxPooling
Encoder Conv3d-3	(Conv96 + ReLU) × 3 + MaxPooling
Encoder Conv3d-4	(Conv96 + ReLU) × 3
Encoder FC	2592 + ReLU → 1000 + ReLU → 100
Mean, Variance, Latent vector	100
Decoder	
Decoder FC	100 + ReLU → 1000 + ReLU → 2592
Decoder ConvTranspose3d-1	(Conv96 + ReLU) × 3 + Upsampling
Decoder ConvTranspose3d-2	(Conv64 + ReLU) × 3 + Upsampling
Decoder ConvTranspose3d-3	(Conv32 + ReLU) × 3 + Upsampling
Decoder ConvTranspose3d-4	(Conv16 + ReLU) × 2 + Conv1 + Sigmoid
Regressor for mechanical properties	
Regressor-mechanical FC	1000 + ReLU → 500 + ReLU → 100 + ReLU → 4
Regressor for manufacturability metrics	
Regressor-manufacturability FC	1000 + ReLU → 500 + ReLU → 100 + ReLU → 5
Discriminator for manufacturability metrics	
Discriminator FC	1000 + ReLU → 500 + ReLU → 100 + Sigmoid → 2

Multi-objective design optimization: manufacturability metric values and true manufacturability of the optimal design candidates

See Table 7 and Fig. 13

Table 7 Manufacturability constraints and true manufacturability metric values of the optimal design candidates

Design candidates	Manufacturability													
	$SA(\mathrm{mm}^2)$		$\frac{SA}{V}(\mathrm{mm}^{-1})$		$L(\mathrm{mm})$		$\theta(°)$		$t_{\max}(\mathrm{mm})$		EV		$L_{\text{connectivity}}$	
Metrics value	≤12000		≤0.5		≤10		≥10		≤20		0		0	
	P	*T*	*P*	*T*	*P*	*T*	*P*	*T*	*P*	*T*	*P*	*T*	*P*	*T*
#1	5718	5952	0.20	0.19	8.4	9.899	10.8	5.7682	4.9	5.1962	0	0	0	0
#2	5899	6096	0.19	0.19	5.2	4	15.0	14.036	5.9	5.1539	0	0	0	0
#3	5707	6192	0.20	0.19	3.7	4	12.4	14.036	6.6	6.2539	0	0	0	0
#4	5630	6336	0.23	0.20	4.7	4	15.8	14.036	5.0	5.1539	0	0	0	0
#5	5644	6360	0.22	0.20	4.0	5	13.3	11.31	6.8	6.8935	0	0	0	0
#6	5134	6552	0.29	0.24	4.7	5	12.4	11.31	6.4	6.1188	0	0	0	0
#7	5825	6696	0.25	0.21	6.1	6	11.3	9.4623	4.7	4.9889	0	0	0	0
#8	6989	6864	0.37	0.32	4.7	5	13.3	11.31	7.2	6.9282	0	0	0	0
#9	5411	6888	0.21	0.21	8.1	8.485	10.1	6.7214	6.6	6.25	0	0	0	0
#10	10030	9096	0.28	0.29	6.2	6	11.4	9.4623	7.1	6.2539	0	0	0	0
#11	11320	9744	0.30	0.30	3.3	4	15.6	14.036	7.4	6.9282	0	0	0	0
#12	8774	9840	0.30	0.31	5.2	5	15.5	11.31	7.1	7.6837	0	0	0	0
#13	7831	9864	0.30	0.31	6.8	6	13.3	9.4623	7.9	7.5	0	0	0	0
#14	9085	9984	0.27	0.31	2.2	2.236	28.5	24.095	6.4	6.7315	0	0	0	0
#15	9776	9864	0.35	0.31	1.2	2	30.2	26.565	6.9	6.2539	0	0	0	0
#16	9076	10104	0.16	0.21	6.9	7	10.4	8.1301	7.5	7.5	0	0	0	0
#17	11790	10512	0.33	0.34	4.7	4	15.5	14.036	6.7	6.2539	0	0	0	0
#18	9437	10416	0.38	0.33	3.0	2.828	22.8	19.471	6.7	6.3738	0	0	0	0
#19	11038	11160	0.31	0.35	5.5	6	13.2	9.4623	6.4	6.2539	0	0	0	0
#20	9907	11184	0.34	0.35	1.5	2.236	25.8	24.095	6.1	6.3738	0	0	0	0

P represents predicted values from supervised learning models and *T* represents ground truth value obtained by image analysis on the structures. The design candidates satisfying all manufacturability constraints are highlighted in gray

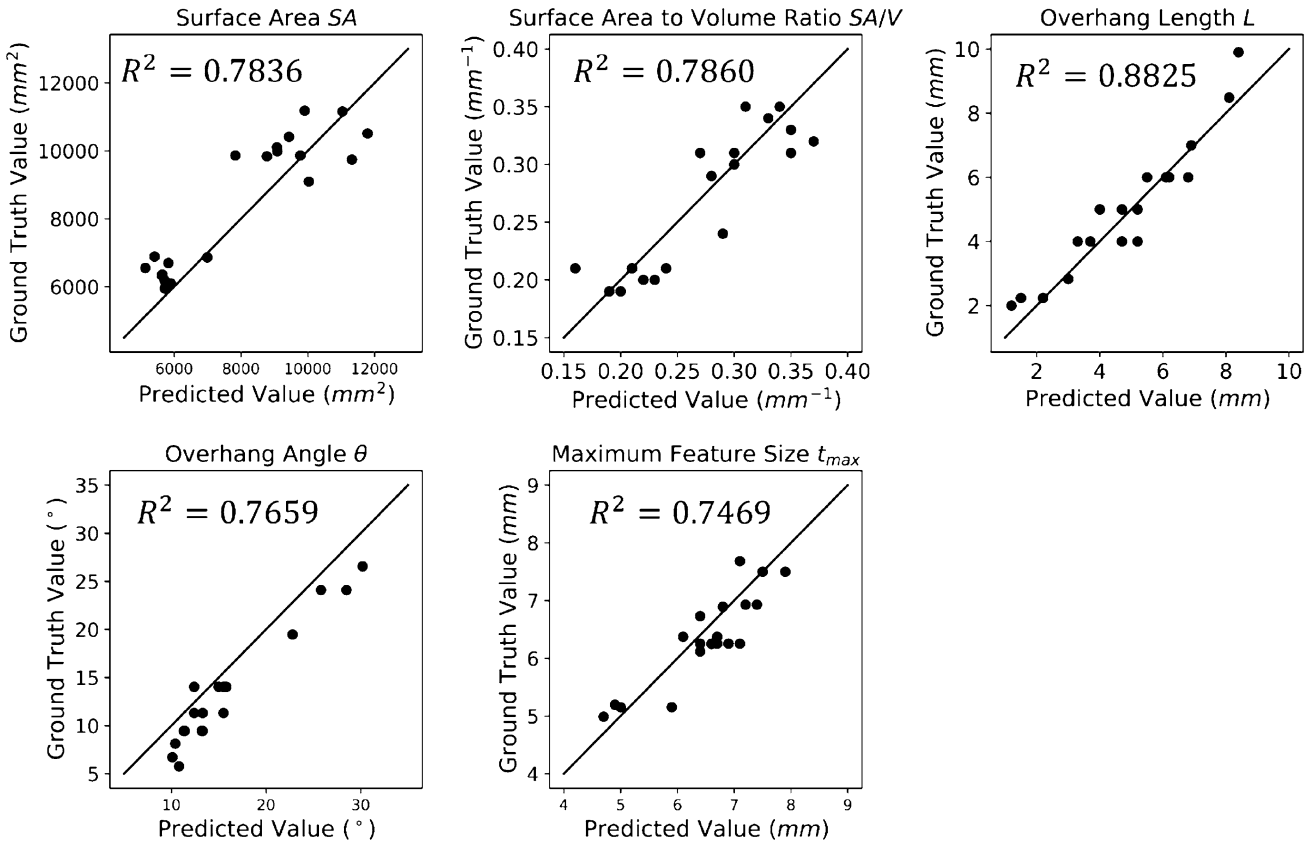

Fig. 13 True manufacturability metrics values and the predicted values by the supervised learning model

Acknowledgements This material is based upon works supported by the National Science Foundation (NSF) under Grant No. IIP-#1822157 (Phase I IUCRC at University of Connecticut: Center for Science of Heterogeneous Additive Printing of 3D Materials, SHAP3D) and NSF Grant No. CMMI-2142290. Any opinions, findings, and conclusions or recommendations expressed in this material are those of the author(s) and do not necessarily reflect the views of the National Science Foundation or the sponsors.

Declarations

Conflict of interest The authors declare that they have no conflicts of interest.

Replication of results Upon acceptance, the authors will provide access to the data and model required to reproduce the results upon reasonable request.

References

Alberdi R, Dingreville R, Robbins J, Walsh T, White BC, Jared B, Boyce BL (2020) Multi-morphology lattices lead to improved plastic energy absorption. Mater Des 194:108883

Ashburner J, Friston KJ (2000) Voxel-based morphometry—the methods. Neuroimage 11(6):805–821

Atzeni E, Salmi A (2015) Study on unsupported overhangs of AlSi10Mg parts processed by Direct Metal Laser Sintering (DMLS). J Manuf Process 20:500–506

Babaee S, Shim J, Weaver JC, Chen ER, Patel N, Bertoldi K (2013) 3D soft metamaterials with negative Poisson's ratio. Adv Mater 25(36):5044–5049

Bastek J-H, Kumar S, Telgen B, Glaesener RN, Kochmann DM (2022) Inverting the structure–property map of truss metamaterials by deep learning. Proc Natl Acad Sci 119(1):e2111505119

Bertrand P, Bayle F, Combe C, Gœuriot P, Smurov I (2007) Ceramic components manufacturing by selective laser sintering. Appl Surf Sci 254(4):989–992

Bintara RD, Aminnudin A, Prasetiyo D, Arbianto FR (2019) The characteristic of overhang object to material usage on FDM 3D printing technology. J Mech Eng Sci Technol (JMEST) 3(1):35–41

Bodaghi M, Damanpack A, Hu G, Liao W (2017) Large deformations of soft metamaterials fabricated by 3D printing. Mater Des 131:81–91

Booth JW, Alperovich J, Chawla P, Ma J, Reid TN, Ramani K (2017) The design for additive manufacturing worksheet. J Mech Des 139(10):100904

Boschetto A, Bottini L (2014) Accuracy prediction in fused deposition modeling. Int J Adv Manuf Technol 73(5):913–928

Bostanabad R, Chan Y-C, Wang L, Zhu P, Chen W (2019) Globally approximate gaussian processes for big data with application to data-driven metamaterials design. J Mech Des 141(11):111402

Cang R, Xu Y, Chen S, Liu Y, Jiao Y, Yi Ren M (2017) Microstructure representation and reconstruction of heterogeneous materials via deep belief network for computational material design. J Mech Des. https://doi.org/10.1115/1.4036649

Cao S, Qiu Y, Wei X-F, Zhang H-H (2015) Experimental and theoretical investigation on ultra-thin powder layering in three dimensional printing (3DP) by a novel double-smoothing mechanism. J Mater Process Technol 220:231–242

Chan Y-C, Ahmed F, Wang L, Chen W (2021) METASET: exploring shape and property spaces for data-driven metamaterials design. J Mech Des 143(3):031707

Chen H, Chan CT (2007) Acoustic cloaking in three dimensions using acoustic metamaterials. Appl Phys Lett 91(18):183518

Chen D, Skouras M, Zhu B, Matusik W (2018) Computational discovery of extremal microstructure families. Sci Adv 4(1):eaao7005

Claeys C, de Melo Filho NGR, Van Belle L, Deckers E, Desmet W (2017) Design and validation of metamaterials for multiple structural stop bands in waveguides. Extreme Mech Lett 12:7–22

Evans KE (1991) Auxetic polymers: a new range of materials. Endeavour 15(4):170–174

Feng S, Kamat AM, Sabooni S, Pei Y (2021) Experimental and numerical investigation of the origin of surface roughness in laser powder bed fused overhang regions. Virtual Phys Prototyping 16(sup1):S66–S84

Gao J, Li H, Gao L, Xiao M (2018) Topological shape optimization of 3D micro-structured materials using energy-based homogenization method. Adv Eng Softw 116:89–102

Garland AP, Adstedt KM, Casias ZJ, White BC, Mook WM, Kaehr B, Jared BH, Lester BT, Leathe NS, Schwaller E (2020) Coulombic friction in metamaterials to dissipate mechanical energy. Extreme Mech Lett 40:100847

Grasso M, Colosimo BM (2017) Process defects and in situ monitoring methods in metal powder bed fusion: a review. Meas Sci Technol 28(4):044005

Grima JN, Winczewski S, Mizzi L, Grech MC, Cauchi R, Gatt R, Attard D, Wojciechowski KW, Rybicki J (2015) Tailoring graphene to achieve negative Poisson's ratio properties. Adv Mater 27(8):1455–1459

Gu GX, Chen C-T, Richmond DJ, Buehler MJ (2018) Bioinspired hierarchical composite design using machine learning: simulation, additive manufacturing, and experiment. Mater Horiz 5(5):939–945

Gurbuz C, Kronowetter F, Dietz C, Eser M, Schmid J, Marburg S (2021) Generative adversarial networks for the design of acoustic metamaterials. J Acoust Soc Am 149(2):1162

He L, Song X (2018) Supportability of a high-yield-stress slurry in a new stereolithography-based ceramic fabrication process. Jom 70:407–412

Hunter LW, Brackett D, Brierley N, Yang J, Attallah MM (2020) Assessment of trapped powder removal and inspection strategies for powder bed fusion techniques. Int J Adv Manuf Technol 106:4521–4532

Hutmacher DW, Schantz T, Zein I, Ng KW, Teoh SH, Tan KC (2001) Mechanical properties and cell cultural response of polycaprolactone scaffolds designed and fabricated via fused deposition modeling. J Biomed Mater Res 55(2):203–216

Järvinen J-P, Matilainen V, Li X, Piili H, Salminen A, Mäkelä I, Nyrhilä O (2014) Characterization of effect of support structures in laser additive manufacturing of stainless steel. Phys Procedia 56:72–81

Jha D, Singh S, Al-Bahrani R, Liao W-K, Choudhary A, De Graef M, Agrawal A (2018) Extracting grain orientations from ebsd patterns of polycrystalline materials using convolutional neural networks. Microsc Microanal 24(5):497–502

Jiang J, Xu X, Stringer J (2018) Support structures for additive manufacturing: a review. J Manuf Mater Process 2(4):64

Jin Y, Du J, He Y (2017) Optimization of process planning for reducing material consumption in additive manufacturing. J Manuf Syst 44:65–78

Kerbrat O, Mognol P, Hascoët J-Y (2011) A new DFM approach to combine machining and additive manufacturing. Comput Ind 62(7):684–692

Kingma DP, Welling M (2014) Stochastic gradient VB and the variational auto-encoder. In: Second international conference on learning representations, ICLR

Kruth J-P, Vandenbroucke B, Van Vaerenbergh J, Mercelis P (2005) Benchmarking of different SLS/SLM processes as rapid manufacturing techniques. In: Proceedings of the International conference polymers & moulds innovations PMI 2005

Kumar S, Tan S, Zheng L, Kochmann DM (2020) Inverse-designed spinodoid metamaterials. Npj Comput Mater 6(1):73

Lam TF, Xiong Y, Dharmawan AG, Foong S, Soh GS (2020) Adaptive process control implementation of wire arc additive manufacturing for thin-walled components with overhang features. Int J Adv Manuf Technol 108:1061–1071

Lee J, Lee K (2017) Block-based inner support structure generation algorithm for 3D printing using fused deposition modeling. Int J Adv Manuf Technol 89(5):2151–2163

Lei M, Hong W, Zhao Z, Hamel C, Chen M, Lu H, Qi HJ (2019) 3D printing of auxetic metamaterials with digitally reprogrammable shape. ACS Appl Mater Interfaces 11(25):22768–22776

Li M, Wang Z (2020) Reliability-based multifidelity optimization using adaptive hybrid learning. ASCE-ASME J Risk Uncertain Eng Syst B 6(2):021005

Li S, Hassanin H, Attallah MM, Adkins NJ, Essa K (2016) The development of TiNi-based negative Poisson's ratio structure using selective laser melting. Acta Mater 105:75–83

Li C, Liu J, Fang X, Guo Y (2017) Efficient predictive model of part distortion and residual stress in selective laser melting. Addit Manuf 17:157–168

Li H, Luo Z, Gao L, Qin Q (2018) Topology optimization for concurrent design of structures with multi-patch microstructures by level sets. Comput Methods Appl Mech Eng 331:536–561

Liu R, Agrawal A, Liao W, Choudhary A, De Graef M (2016) Materials discovery: understanding polycrystals from large-scale electron patterns. In: 2016 IEEE International conference on big data (Big Data). IEEE

Liu Z, Xu H, Zhu P (2020) An adaptive multi-fidelity approach for design optimization of mesostructure-structure systems. Struct Multidisc Optim 62:375–386

Lores A, Azurmendi N, Agote I, Zuza E (2019) A review on recent developments in binder jetting metal additive manufacturing: materials and process characteristics. Powder Metall 62(5):267–296

Meyer PP, Bonatti C, Tancogne-Dejean T, Mohr D (2022) Graph-based metamaterials: deep learning of structure-property relations. Mater Des 223:111175

Mirabolghasemi A, Akbarzadeh A, Rodrigue D, Therriault D (2019) Thermal conductivity of architected cellular metamaterials. Acta Mater 174:61–80

Moylan S, Slotwinski J, Cooke A, Jurrens K, Donmez MA (2023) Proposal for a standardized test artifact for additive manufacturing machines and processes. In: 2012 International solid freeform fabrication symposium. University of Texas at Austin

Oliveira JP, LaLonde A, Ma J (2020) Processing parameters in laser powder bed fusion metal additive manufacturing. Mater Des 193:108762

Paszke A, Gross S, Massa F, Lerer A, Bradbury J, Chanan G, Killeen T, Lin Z, Gimelshein N, Antiga L (2019) Pytorch: an imperative style, high-performance deep learning library. In: Advances in neural information processing systems, vol 32

Pham M-S, Liu C, Todd I, Lertthanasarn J (2019) Damage-tolerant architected materials inspired by crystal microstructure. Nature 565(7739):305–311

Qi Z, Zhang N, Liu Y, Chen W (2019) Prediction of mechanical properties of carbon fiber based on cross-scale FEM and machine learning. Compos Struct 212:199–206

Qian X (2017) Undercut and overhang angle control in topology optimization: a density gradient based integral approach. Int J Numer Methods Eng 111(3):247–272

Qian J, Cheng Y, Zhang A, Zhou Q, Zhang J (2021) Optimization design of metamaterial vibration isolator with honeycomb structure based on multi-fidelity surrogate model. Struct Multidisc Optim 64:423–439

Reddy KSN, Ferguson I, Frecker M, Simpson TW, Dickman CJ (2016) Topology optimization software for additive manufacturing: a review of current capabilities and a real-world example. In: International design engineering technical conferences and computers and information in engineering conference. 2016. American Society of Mechanical Engineers

Shi Y, Zhang Y, Baek S, De Backer W, Harik R (2018) Manufacturability analysis for additive manufacturing using a novel feature recognition technique. Comput-Aided Des Appl 15(6):941–952

Strano G, Hao L, Everson R, Evans K (2013) A new approach to the design and optimisation of support structures in additive manufacturing. Int J Adv Manuf Technol 66:1247–1254

Takezawa A, Koizumi Y, Kobashi M (2017) High-stiffness and strength porous maraging steel via topology optimization and selective laser melting. Addit Manuf 18:194–202

Tao W, Leu MC (2016) Design of lattice structure for additive manufacturing. In: 2016 International symposium on flexible automation (ISFA). IEEE

Tedia S, Williams CB (2016) Manufacturability analysis tool for additive manufacturing using voxel-based geometric modeling. In: 2016 International solid freeform fabrication symposium. University of Texas at Austin

Telea A, Jalba A (2011) Voxel-based assessment of printability of 3D shapes. In: Mathematical morphology and its applications to image and signal processing: 10th international symposium, ISMM 2011, Verbania-Intra, Italy, July 6–8, 2011. Proceedings 10. Springer

Thompson MK, Moroni G, Vaneker T, Fadel G, Campbell RI, Gibson I, Bernard A, Schulz J, Graf P, Ahuja B (2016) Design for additive manufacturing: trends, opportunities, considerations, and constraints. CIRP Ann 65(2):737–760

Thore C-J, Grundström HA, Torstenfelt B, Klarbring A (2019) Penalty regulation of overhang in topology optimization for additive manufacturing. Struct Multidisc Optim 60:59–67

Tuncer N, Bose A (2020) Solid-state metal additive manufacturing: a review. Jom 72(9):3090–3111

Vogiatzis P, Chen S, Wang X, Li T, Wang L (2017) Topology optimization of multi-material negative Poisson's ratio metamaterials using a reconciled level set method. Comput Aided Des 83:15–32

Vogiatzis P, Chen S, Gu XD, Chuang C-H, Xu H, Lei N (2018) Multimaterial topology optimization of structures infilled with conformal metamaterials. In: International design engineering technical conferences and computers and information in engineering conference. American Society of Mechanical Engineers

Walton D, Moztarzadeh H (2017) Design and development of an additive manufactured component by topology optimisation. Procedia Cirp 60:205–210

Wang Y, Luo Z, Zhang N, Kang Z (2014) Topological shape optimization of microstructural metamaterials using a level set method. Comput Mater Sci 87:178–186

Wang C, Xu B, Meng Q, Rong J, Zhao Y (2020a) Numerical performance of Poisson method for restricting enclosed voids in topology optimization. Comput Struct 239:106337

Wang L, Chan Y-C, Liu Z, Zhu P, Chen W (2020b) Data-driven metamaterial design with Laplace-Beltrami spectrum as "shape-DNA." Struct Multidisc Optim 61:2613–2628

Wang Z, Xian W, Baccouche MR, Lanzerath H, Li Y, Xu H (2021) A Gaussian mixture variational autoencoder-based approach for designing phononic bandgap metamaterials. In: International design engineering technical conferences and computers and information in engineering conference. American Society of Mechanical Engineers

Wang Z, Xian W, Baccouche MR, Lanzerath H, Li Y, Xu H (2022a) Design of phononic bandgap metamaterials based on Gaussian mixture beta variational autoencoder and iterative model updating. J Mech Des 144(4):041705

Wang Z, Zhuang R, Xian W, Tian J, Li Y, Chen S, Xu H (2022b) Phononic metamaterial design via transfer learning-based topology optimization framework. In: International design engineering technical conferences and computers and information in engineering conference. American Society of Mechanical Engineers

Watts S, Arrighi W, Kudo J, Tortorelli DA, White DA (2019) Simple, accurate surrogate models of the elastic response of three-dimensional open truss micro-architectures with applications to multiscale topology design. Struct Multidisc Optim 60(5):1887–1920

Wei X, Geng G, Zhang Y (2016) Steady and low consuming supporting for fused deposition modeling. Zidonghua Xuebao/acta Automatica Sinica 42(1):98–106

Wei C, Chueh Y-H, Zhang X, Huang Y, Chen Q, Li L (2019) Easy-to-remove composite support material and procedure in additive manufacturing of metallic components using multiple material laser-based powder bed fusion. J Manuf Sci Eng. https://doi.org/10.1115/1.4043536

White T (2016) Sampling generative networks. arXiv preprint arXiv:1609.04468

Wilt JK, Yang C, Gu GX (2020) Accelerating auxetic metamaterial design with deep learning. Adv Eng Mater 22(5):1901266

Xia Z, Zhang Y, Ellyin F (2003) A unified periodical boundary conditions for representative volume elements of composites and applications. Int J Solids Struct 40(8):1907–1921

Xiong Y, Yao S, Zhao Z-L, Xie YM (2020) A new approach to eliminating enclosed voids in topology optimization for additive manufacturing. Addit Manuf 32:101006

Xu H, Liu Z (2019) Control variate multifidelity estimators for the variance and sensitivity analysis of mesostructure–structure systems. ASCE-ASME J Risk Uncertain Eng Syst B 5(2):020907

Xu L, Hoffman N, Wang Z, Xu H (2022) Harnessing structural stochasticity in the computational discovery and design of microstructures. Mater Des 223:111223

Yadollahi A, Shamsaei N (2017) Additive manufacturing of fatigue resistant materials: challenges and opportunities. Int J Fatigue 98:14–31

Yang KV, Rometsch P, Jarvis T, Rao J, Cao S, Davies C, Wu X (2018) Porosity formation mechanisms and fatigue response in Al-Si-Mg alloys made by selective laser melting. Mater Sci Eng A 712:166–174

Yasuda H, Yang J (2015) Reentrant origami-based metamaterials with negative Poisson's ratio and bistability. Phys Rev Lett 114(18):185502

Zein I, Hutmacher DW, Tan KC, Teoh SH (2002) Fused deposition modeling of novel scaffold architectures for tissue engineering applications. Biomaterials 23(4):1169–1185

Zeng Q, Zhao Z, Lei H, Wang P (2022) A deep learning approach for reverse design of gradient mechanical metamaterials. Int J Mech Sci 240:107920

Zeng Q, Zhao Z, Lei H, Wang P (2023) A deep learning approach for inverse design of gradient mechanical metamaterials. Int J Mech Sci 240:107920

Zhang G, Khandelwal K (2020) Topology optimization of dissipative metamaterials at finite strains based on nonlinear homogenization. Struct Multidisc Optim 62:1419–1455

Zhang Y, Yang S, Zhao YF (2020) Manufacturability analysis of metal laser-based powder bed fusion additive manufacturing—a survey. Int J Adv Manuf Technol 110(1):57–78

Zhang K, Cheng G, Wang Y (2022a) Structural topology optimization subject to overhang angle constraint with overhang length relaxation in additive manufacturing. Sci China Technol Sci 65(6):1213–1231

Zhang W, Wang C, Zhou L, Gao T (2022b) Three-dimensional topology optimization considering overhang constraints with B-spline parameterization. Comput Struct 269:106823

Zheng X, Lee H, Weisgraber TH, Shusteff M, DeOtte J, Duoss EB, Kuntz JD, Biener MM, Ge Q, Jackson JA (2014) Ultralight, ultrastiff mechanical metamaterials. Science 344(6190):1373–1377

Zhou L, Zhang W (2019) Topology optimization method with elimination of enclosed voids. Struct Multidisc Optim 60:117–136